Mineralogy and Petrology (2007) 91: 71–100
DOI 10.1007/s00710-007-0182-8
Printed in The Netherlands

Mineralogy and Petrology

The nature and origin of Fe-Ti-P-rich rocks in the Qareaghaj mafic-ultramafic intrusion, NW Iran

M. Mirmohammadi[1], **A. Kananian**[1], and **M. Tarkian**[2]

[1] School of Geology, University College of Science, Tehran University, Tehran, Iran
[2] Institute of Mineralogy and Petrology, University of Hamburg, Hamburg, Germany

Received March 30, 2006; revised version accepted January 1, 2007
Published online February 22, 2007;
Editorial handling: S. Maaløe

Summary

Fe-Ti-P-rich rocks (FTP) are unusual with respect to their mineralogy and bulk composition. Varieties of these rocks are mostly related to Proterozoic massif-type anorthosites and to a lesser extent to the upper parts of mafic-ultramafic intracratonic layered complexes and other igneous rock suites. We present results on the geology, mineralogy and geochemistry of a new occurrence of FTP, associated with mafic rocks in the northwestern part of Iran. The Qareaghaj mafic-ultramafic intrusion (QMUI) is a small igneous body situated between Palaeozoic sedimentary rocks and a Precambrian low grade metamorphic complex. The QMUI is composed mainly of non-mineralized mafic and apatite- and Fe-Ti oxide-rich ultramafic rocks. The mafic rocks, mainly coarse-grained gabbro, microgabbro and amphibolite, have a simple mineral assemblage (plagioclase + clinopyroxene + ilmenite) and based on field observations, mineralogy and chemical composition are comagmatic. The ultramafic rocks with high proportion of olivine (~ 40–66 vol.%), apatite (~ 0.1–16 vol.%), ilmenite (~ 11–19 vol.%) and magnetite (~ 2–13 vol.%), have unusual bulk compositions (e.g., SiO_2 ~ 21–30 wt.%, total iron expressed as $Fe_2O_3{}^{tot}$ ~ 26–42 wt.%, TiO_2 ~ 5–11 wt.%, MgO ~ 9–20 wt.%, P_2O_5 up to 5.1 wt.%, Cr ~ 40–160 ppm, Ni ~ 7–73 ppm). The FTP forms numerous sill-like layers, ranging in thickness from ~5 cm to few meters. These rocks, totally enclosed in mafic rocks with sharp and concordant contacts, show a magmatic lamination and follow the general NW–SE trend of QMUI. The apatite-rich ultramafic rocks makes up 90–95% of the total ultramafic outcrops and contain Mg-poor olivine (Mg# ~ 40–58) and low-Mg spinel (Mg# ~ 30–44) in contrast to apatite-poor ones (~60–63 and ~43–46, respectively). Field relationships, mineral compositions and geochemical data suggested that the FTP are not related to the mafic host rocks. On the contrary, they intruded latter into the gabbros during plastic, high temperature

deformation in local shear zones. Fractional crystallization of P-rich ferrobasaltic parental magma at depth, probably in an open magmatic system, not far from the QMUI magma chamber, is considered as responsible for the formation of the evolved FTP in QMUI.

Introduction

Although Fe-Ti-P-rich rocks (FTP) are generally volumetrically minor, they have a considerable importance because of their (i) potential as Fe-Ti oxide and apatite ores, (ii) unusual bulk composition and mineral assemblage compared to common igneous rocks (*Owens* and *Dymek*, 1992) and (iii) petrogenetic constraint to various magmatic host rocks.

These rocks are commonly found in the form of sills, dikes, sheets, pods, lens-like and massive concordant or disconcordant bodies (e.g., *Kolker*, 1982; *McLelland* et al., 1994; *Owens* and *Dymek*, 1992; *Duchesne*, 1999) and composed of various proportions of Fe-Ti oxides, apatite, pyroxenes and olivine with/without accessory phases such as sulfides, hercynitic spinel and biotite.

A wide variety of FTP has been reported in association with Proterozoic massif-type anorthosites (e.g., *Philpotts*, 1967; *Ashwal*, 1993; *Owens* and *Dymek*, 1992; *Markl* et al., 1998; *Duchesne*, 1999; *Arebäck* and *Stigh*, 2000) and to a lesser extent with alkaline igneous complexes (*Force*, 1991; *Jiang* et al., 2004), the upper parts of layered mafic-ultramafic intrusions such as Bushveld (e.g., *Reynolds*, 1985a; *Von Gruenewaldt*, 1993; *Lee*, 1996), Skaergaard (*Larsen* and *Brooks*, 1994; *McBirney*, 1996), Duluth complex (e.g., *Severson*, 1988; *Rippley* et al., 1998), and also in small gabbroic layered intrusions in Finland (*Kärkkäinen* and *Appelqvist*, 1999; *Kärkkäinen* and *Bornhorst*, 2003).

The FTP are known by many different names, based on mineralogy and composition, such as nelsonite (*Watson* and *Taber*, 1913; *Philpotts*, 1967), jotunite and oxide-apatite gabbronorite (OAGN; *Owens* and *Dymek*, 1992), ferrogabbro, ferrodiorite and oxide-rich ultramafic intrusions (OUI; *Severson*, 1988).

A variety of hypotheses has been proposed for the origin of FTP (e.g., *Kolker*, 1982; *Reynolds*, 1985b; *Force*, 1991; *Owens* and *Dymek*, 1992; *Duchesne*, 1999). However, there is no consensus on the relationships among various FTP and their petrogenesis (*Dymek* and *Owens*, 2001).

Qareaghaj mafic-ultramafic intrusion (QMUI) is one occurrence of FTP rocks located in NW Iran and was discovered in 1993. This intrusion is relatively small in size ($\sim$ 8–10 km long and 1–1.7 km wide, Fig. 1). The geology, mineralization and lab-scale mineral processing were studied when the QMUI was explored for titanium and phosphorus (*Emamalipour* and *Masoudi*, 1996; *Kavoshgaran*, 1996). The QMUI mainly consists of non-mineralized gabbro and amphibolite, and apatite- and Fe-Ti oxide-rich ultramafic rocks.

In Iran, Kahnooj is the only known ilmenite deposit (placer type from gabbroic rock source) which is located in southern Iran. On the other hand, there are many large magnetite ($\pm$apatite) ore deposits (e.g., Gole Gohar, Bafg, Chogart and Sangan), mainly situated in the Sanandaj-Sirjan and Central Iran structural zones. Most of these ores, associated with ultramafic, calc-alkaline and other rock suites with significant carbonate enrichment, have been considered as Kiruna-type deposits

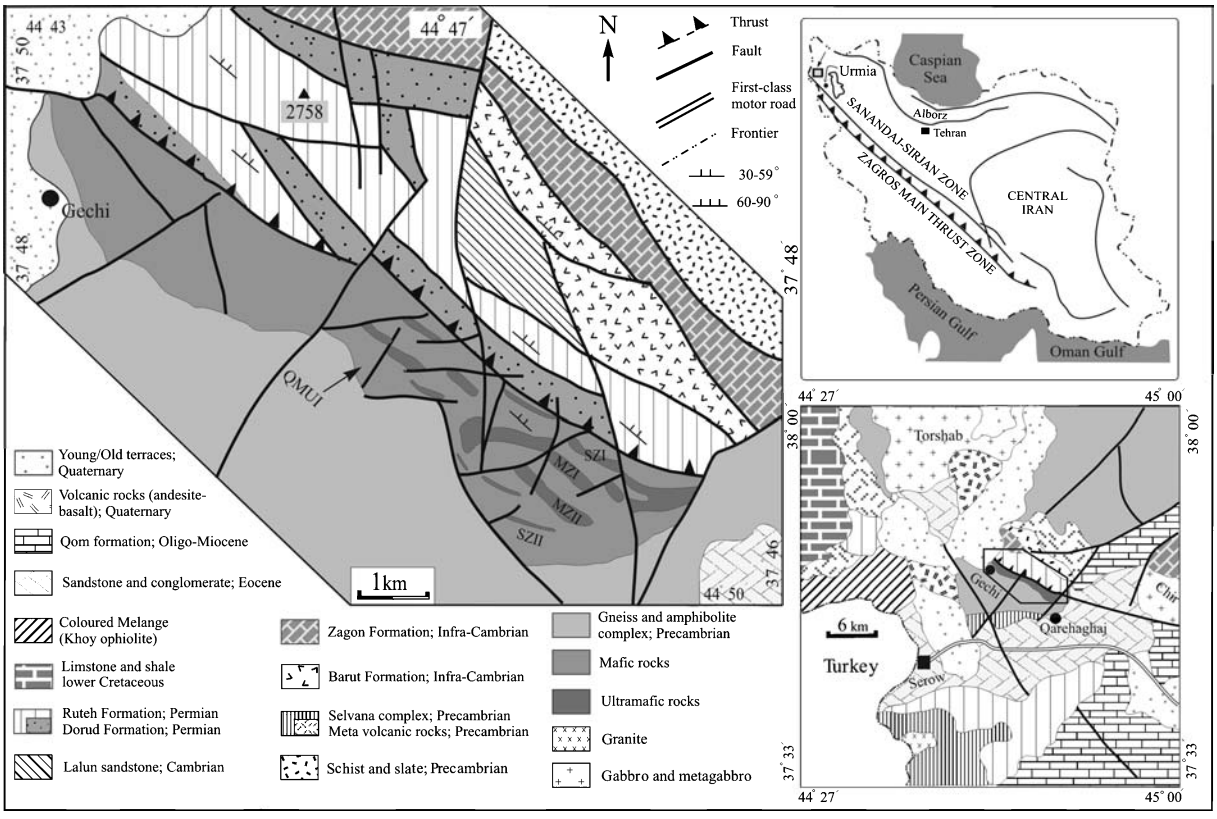

Fig. 1. Location and generalized geological map of QMUI area (modified after *Haghipour* and *Aghanabati*, 1973; *Emamalipour* and *Masoudi*, 1996)

(*Daliran* and *Amstutz*, 1991; *Mücke* and *Younessi*, 1994; *Förster* and *Jafarzadeh*, 1994). Hence, QMUI is the only ilmenite-bearing FTP occurrence in Iran, so far, and its mineralogy and host rock relationships show some distinct differences from the other FTP in the world.

In this paper we present, for the first time, the results of detailed geology, mineralogy and geochemical characteristics of the QMUI. Although, the paper is focused on apatite- and Fe-Ti oxide-rich ultramafic parts of the intrusion, relationships and features of the associated rock types are also discussed. In an attempt to clarify the petrogenesis of the FTP, we discuss the nature and origin of the QMUI and describe its similarities and differences with some of the known FTP from igneous suites in the world.

Regional geology

The studied area is located in northwest Iran, 36 km NW from Urmia city, close to the Iran-Turkey border (Fig. 1) and considered as a part of the Khoy-Mahabad structural subzone. Indeed, this area can be considered as a junction of three main structural zones including those of Alborz-Azerbaijan, Central Iran and Sanandaj-Sirjan (Fig. 1). The geological development of these zones has pre-

viously been reviewed by *Stöklin* (1974), *Davoudzadeh* and *Weber Diefenbach* (1986).

The QMUI is situated between Permian and Infracambrian-Cambrian sequences, composed mainly of sedimentary and low grade metamorphic rocks on the north and Precambrian metamorphic complexes to the south and east (Fig. 1). However a few Rb-Sr ages of 663 Ma and 1.56 Ga were reported for the metarhyolite unit of Kahar formation (*Crawford*, 1977) and Selvana complexes (*Haghipour* and *Aghanabati*, 1973), respectively, which are close to the study area. The Infracambrian-Cambrian rocks include Barut and Zaigun Formations, Lalun sandstone, Mila dolomite and limestone, mainly located on the north of the QMUI. Rocks of Ordovician age are restricted to small outcrops and rocks from Silurian through Carboniferous are totally absent. The Permian, red quartzo-feldspathic sandstone (Durud Formation), and limestone-dolomitic limestone (Ruthe Formation), have a fault contact with the northern margin of the QMUI (Fig. 1). Triassic and Jurassic sequences are absent, while Cretaceous rocks include a thick sequences of flysch and the Khoy ophiolitic complex (*Hassanipak* and *Ghazi*, 2000). The youngest, Quaternary, rocks and sediments are composed of andesitic-basaltic lavas, travertine terraces and gravel fans, mainly located in the northwest. Other intrusions, which are generally larger than QMUI, are also exposed near the study area. These intrusions (e.g., Chir and Torshan; Fig. 1) are commonly composed of medium- to coarse-grained gabbro, metagabbro and amphibolite. Petrography and field features of one of these intrusions (Chir) shows some similarities to the mafic part of the QMUI, although FTP rocks were not observed.

Field relationships

The QMUI is a relatively small body (about 12 km^2) that generally dips 50–65° N–NE and extends NW–SE (Fig. 1). The hanging-wall country rocks, including a Permian sedimentary sequence, have a fault contact with the intrusion. This contact steeply dips N–NE and is interpreted as a thrust fault which is characterized by a 5–10 m thick mylonite-ultramylonite zone. The foot-wall country rocks include Precambrian quartzo-feldspathic gneiss (mylonitic granite), metavolcanics and, in places, Kahar low-grade metamorphic rocks, having transition contacts in most places, but also fault contacts in others (Fig. 1).

Based on the petrography and mineralogy, QMUI is composed of two main rock types: un-mineralized mafic, the most voluminous type, and ultramafic rocks. Most of the latter are located within the intrusion and enclosed within the mafic rocks. The mafic rocks are mainly gabbros that are deformed and metamorphosed to metagabbro and amphibolite, in particular close to other country rocks. Foliation is a common feature in the mafic part of the intrusion, which is identified by alternating bands enriched in mafic minerals and plagioclase. The gabbros are generally coarse-to medium-grained and locally show pegmatitic facies. Microgabbros, which are the second most voluminous mafic rocks, are characterized by high clinopyroxene content giving them a dark-green color in the field. They appear to crosscut the granular coarse-grained gabbros, whereas the relationships with the ultramafic rocks are unclear. However, at the microscopic scale the contacts are

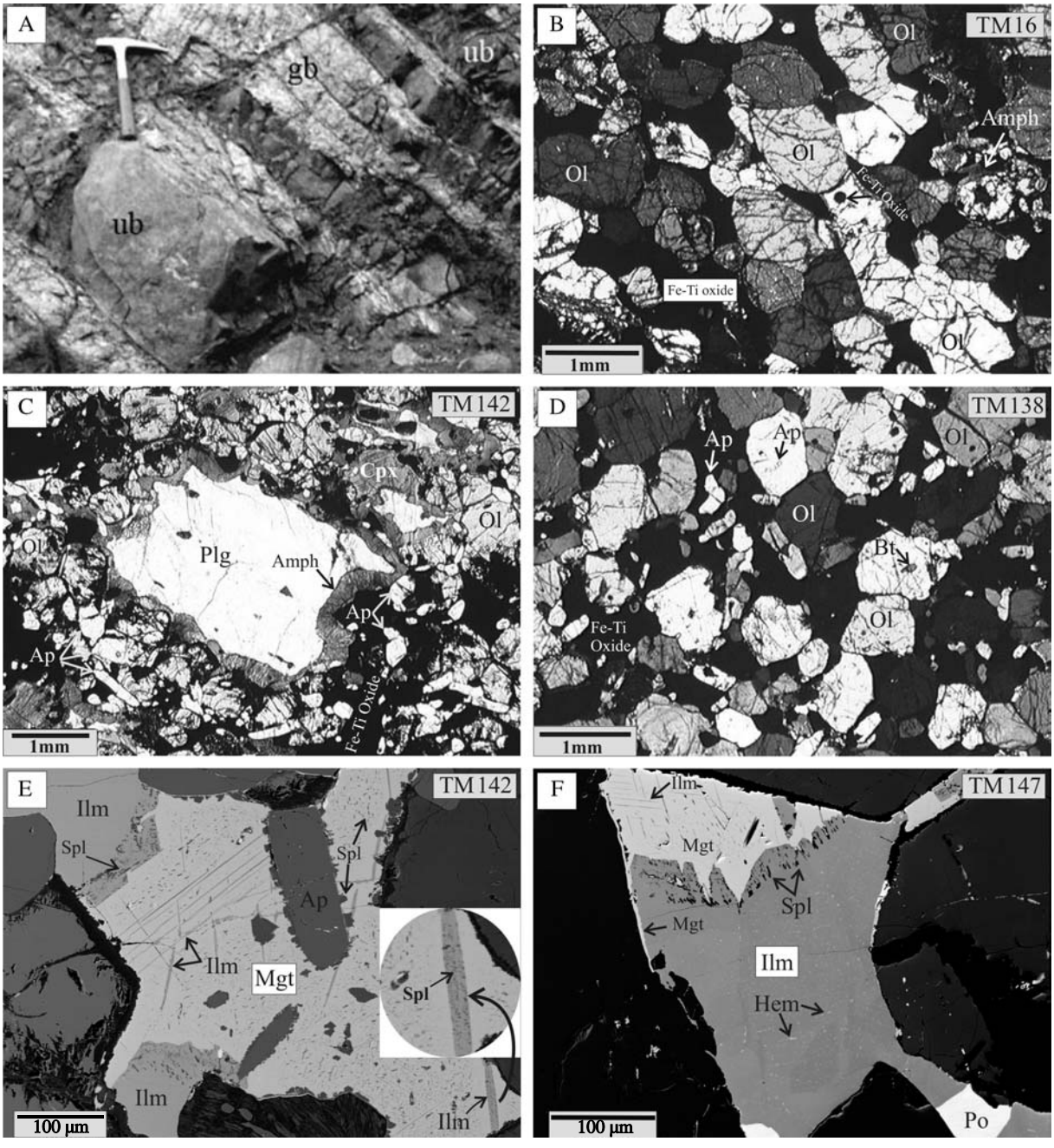

Fig. 2. (A) Field photograph, showing sharp and parallel contacts between ultramafic rocks (ub) and gabbros (gb) in the QMUI. (B) Apatite-poor dunite. A planar fabric is defined by the elongation of the olivine and Fe-Ti oxides. Triple junctions are common between olivine grains. (C) Apatite-oxide-rich wehrlite with large plagioclase xenocryst that is rimmed by amphibole. (D) Net-textured apatite-oxide-rich dunite. (E) and (F) BSE images of Fe-Ti oxide minerals. (B) and (D) were taken under transmitted light with crossed polars; (C) under plane-polarized light. *Ol* Olivine; *Amph* amphibole; *Plag* plagioclase; *Ap* apatite, *Cpx* clinopyroxene; *Bt* biotite; *Ilm* ilmenite; *Mgt* magnetite; *Spl* spinel; *Hem* hematite, *Po* pyrrhotite

mostly sharp. In the field, transitions from granular gabbro to foliated gabbro, metagabbro and amphibolite are very irregular.

The ultramafic rocks are discontinuous sill-like and/or tabular layers that alternate with mafic rocks (Figs. 1 and 2A) and follow the regional trend of the QMUI, as well as the internal structure of the intrusion (e.g., foliation and layering in the mafic rocks). According to field observations, the contacts between mafic and ultramafic rocks are always sharp and concordant (Fig. 2A). Ultramafic apophyses penetrating mafic host rocks are not seen in the field. On the other hand, ultramafic microapophyses in gabbros as well as small gabbroic xenoliths, and plagioclase (and rarely clinopyroxene) xenocrysts in ultramafic rocks are locally observed at the microscopic scale, particularly close to contact zones (Fig. 2C). There are no intermediate compositions between the two main rock types in the whole intrusion. Based on field relationships, the ultramafic rocks are divided into two main zones (MZI and MZII) and two subzones (SZI and SZII, Fig. 1). They are parallel to each other and follow the general trend of the intrusion as well as the foliation in the mafic rocks. The MZI has a total thickness of 30–50 m and contains ~15 unmineralized gabbroic layers (~ 10 cm to 2 m thick). The MZII does not contain any gabbroic layers and the total thickness is from 30 to 60 m. Furthermore, a 1.5 m thick alkali feldspar granite occurs as a layer in the center of MZII and has semi-parallel and sharp contacts. The two subzones are located in the upper and lower part of the intrusion, and are composed of alternating layers of mafic and utramafic rocks (~ 5–50 cm thick) with parallel sharp contacts. Despite extensive alteration, deformation and metamorphism of the mafic rocks, the ultramafic rocks are mostly undeformed and fresh, except along local fractures and shear zones where olivine is mainly altered to serpentine. The ultramafic rocks are also partly altered to iddingsite, and show a brownish color due to concentration of secondary iron oxides and hydroxides at the surface levels. The ultramafic rocks have limited extensions (~ 3.5–4 km long) in the QMUI and are totally included in mafic rocks. The QMUI is cut and dislocated by steeply dipping NW–SE and NE–SW faults. Locally the mafic rocks are cut by highly-altered feldspathic dikes (up to 2 m thick).

Sampling and analytical methods

Samples were collected systematically from outcrops as well as trenches throughout the intrusion. Additional samples (BH code) were also selected from drill cores acquired during previous exploration carried out by the Iranian Ministry of Industries and Mines from 1994 to 1996. Modal abundances of mineral assemblages were determined by point-counting a minimum of 1200 points per section (Table 1). Whole rock major- and trace-element compositions, including REE, of 50 samples were determined at ALS Chemex, Vancouver, Canada, by ICP-AES and ICP-MS, respectively. Analytical precisions are estimated to be better than ±5% for major oxides and ±10% for all of trace elements. Electron microprobe analyses were performed on a CAMECA SX-100, at the Institute of Mineralogy and Petrology of the University of Hamburg, Germany. Both natural and synthetic standards were used for calibration. The beam current was 15 nA for plagioclase and apatite, 20 nA for Fe-Ti oxides and other silicates with acceleration voltage of 15–20 kV. Beam

Table 1. *Representative modal composition (vol.%) of different rock types from QMUI. ox-ub: Oxide-rich (apatite-poor) ultramafic, ap-ox-ub: apatite-oxide-rich ultramafic, hyb: hybrid rocks, mgb: microgabbro, cgb: coarse-grained gabbro, mgr: mylonitic granite, T: trace amounts*

Rock type	ox-ub		ap-ox-ub							hyb	mgb	cgb	
Sample no.	TM16	TM62	TM17	TM46	TM61	TM65	TM134	TM138	TM147	BH2-34	BH1-14	TM18	TM35
Olivine	61.5	46.3	45.6	53.8	54.5	58.4	46	51.7	52	32.6			
Clinopyroxene		12.2	17.2	9.6	3.9	4.2	15.5	4.8	4.4	5.8	45.7	20.3	18
Apatite	0.1	T	12.3	12.7	16.2	13	13.5	12.7	13	12.7		0.1	T
Spinel	0.5	0.9	0.5		0.6	1.2	0.5	0.2	0.3	0.2			
Plagioclase	1.3	11.8				T			2.3	25.5	38.2	66	74.3
Hornblende	4.5	6.8	1.5	1.5	2.8	2.2	2.3	2	3	7.1		3.4	
Serpentine	5.5			0.5				2.4	0.5				
Tremolite-Actinolite	1.8										9.8	4.3	3.7
Chlorite									0.4	3.6	1.2	0.5	
Biotite			0.1	0.1	0.1	0.3	0.2	0.5	0.5				
Total non opaque	75.2	79	77.2	78.2	78.1	79.3	78	74.3	76.4	87.5	94.9	94.6	96
Ilmenite	18	18.8	11.8	11.4	13.8	16.3	15	15.5	16.8	9.2	4.9	5.4	4
Magnetite	6.4	2.2	11	10.4	8.1	4.4	7	7.9	4.5	2.1			
Sulfide	0.4		T	T	T	T	T	2.3	2.3	1.2	0.2		
Total opaque	24.8	21	22.8	21.8	21.8	20.7	22	25.7	23.6	12.5	5.1	5.4	4

size was 10 and 20 μm for plagioclase and apatite and typically 1 μm for other minerals. In addition to the standard microprobe analyses of mineral phases, selected REEs, including La, Ce and Nd in apatite were obtained using the same microprobe. A beam current of 200 nA, an accelerating voltage of 30 kV and a counting time of 240 seconds were used for trace elements. The bulk composition of finely oxy-exsolved titanomagnetite and also ilmenite with hematite exsolutions were measured with a defocused beam of 40 μm.

Petrography

A total of about 150 samples were examined in transmitted and reflected light. The modal compositions of 13 representative samples are given in Table 1.

Ultramafic rocks

These rocks are mostly fine- to medium-grained and show cumulate texture with a framework of olivine and clinopyroxene grains surrounded by interstitial Fe-Ti oxides and apatite (Fig. 2B–D). The most frequent rocks are apatite- and Fe-Ti oxide-rich dunite and wehrlite. However, apatite-poor dunite and clinopyroxenite are also present. Olivine is the most abundant primary cumulus phase ($\sim$40–66 vol.%) and commonly accompanied by trace to 16 vol.% clinopyroxene. Apatite content is high but variable, ranging from trace to 16 vol.%. Plagioclase commonly is found in samples near to the contact of mafic rocks (up to 15 vol.%), but is mostly between 1 and 5 vol.%. Ilmenite ($\sim$ 11–19 vol.%) and Ti-magnetite ($\sim$ 2–13 vol.%) are the common oxides. Accessory minerals include brown hornblende (up to 10 vol.%) as reaction rims (up to 10 μm thick) around other silicates, biotite (<1 vol.%), hercynitic spinel (<1.2 vol.%), sulfide minerals (mainly pyrrhotite and minor chalcopyrite and pentlandite, <3 vol.%). Ilmenite is the dominant Fe-Ti oxide in all of the samples, and apatite is found in about 90–95% of the ultramafic rocks. Although all the samples of ultramafic rocks are apatite-rich, some layers, partly, in MZI and subzones are apatite-poor. The transition from apatite-poor to apatite-rich rocks is gradational to sharp (at the mm to cm scale) which in some cases was recorded in a thin section. Olivine, apatite and clinopyroxene, generally, define a relatively preferred orientation (mineral lamination, Fig. 2B–D) and a weak small scale modal layering in some samples. Mineral lamination, in particular in subzones, is parallel with the contacts of layers, the foliation in the mafic rocks and also the general trend of the intrusion.

Olivine is mostly euhedral to subhedral, nearly equigranular or elongated, ranging in size from 0.2 to 3 mm, and usually includes other phases such as apatite, droplets of oxides and sulfides, biotite (Fig. 2B–D) and rarely zircon. Olivine–olivine grain boundaries usually exhibit a high degree of textural equilibration (polygonal grain boundaries, Fig. 2B–D). In most samples olivine is fresh, although replacement by serpentine ($\pm$ talc $\pm$ chlorite) has been observed at some small localities. Optical zoning is absent in olivine as well as in other silicate minerals.

Clinopyroxene (diopside-augite) is usually subhedral to anhedral and ranges in size from 0.5 to 5 mm. Furthermore, locally small (up to 5 cm thick) patches or thin layers of clinopyroxenite, hosted by dunite or wehrlite are found, which probably

segregated as a consequence of magma flow during emplacement. Clinopyroxene is always free of orthopyroxene exsolution but contains frequent needle-shaped ilmenites, oriented in two directions parallel to the prismatic cleavage, and also apatite, oxides and biotite inclusions. Some olivine and clinopyroxene grains are rimmed by brown hornblende (±biotite, Fig. 2B), suggesting reaction between a hydrous melt and previously crystallized silicate minerals.

Apatite occurs as elongated prismatic euhedral to subhedral grains, 0.05–2 mm in length. It is found in two generations (Fig. 2C–E), large interstitial grains, and small inclusions in olivine, clinopyroxene and Fe-Ti oxides. The apatite/oxide ratio in ultramafic rocks typically is 0.5–0.7.

Plagioclase is subhedral to irregular in shape and ranges in size from 3 to 6 mm in length. Most of the plagioclase grains regarding size (Fig. 2C), shape, twining and also composition (see mineralogy) are similar to plagioclase in gabbros. These features and field observation indicate that most of them are xenocrysts and originated from the gabbros during ultramafic rock emplacement.

The Fe-Ti oxides, ilmenite and Ti-magnetite, are subdivided in three generations (Fig. 2B–F): small rounded to ellipsoidal inclusions in olivine and clinopyroxene, coarse interstitial crystals and late stage veinlets (up to 3 cm thick; mostly pure magnetite ± pyrrhotite). The latter cut silicates and also early crystallized oxides. Ilmenite is the dominant oxide phase; the ilmenite/magnetite ratio generally is 2–4 (range from 1.5 to 8.5). The primary ilmenite grains (0.1–2 mm) commonly contain hematite (titanian hematite) lenses (Fig. 2F), arranged in [0001] planes. Primary Ti-magnetite contains ilmenite lamellae along the [111] planes and exhibits wide variety of exsolution textures (Fig. 2E, F). Trellis-type (both coarse and fine) is more common; however composite- and sandwich-types also occur. Based on microtexture, most of the composite grains probably are primary ilmenite-magnetite pairs. In contrast to the requirement of the oxidation-exsolution model (*Buddington* and *Lindsley*, 1964), the ilmenite lamellae often show a homogenous distribution and are concentrated in the core of the magnetite host, as reported by *Mücke* (2003). Following the classification of textural stages (C1–C5) caused by subsolidus exsolution with increasing degree of oxidation (*Haggerty*, 1991), Ti-magnetites in the ultramafic rocks of QMUI belong to stage C2–C3 without ulvite exsolution. Ti-magnetite, in addition to ilmenite lamellae, mostly contains exsolutions of hercynitic spinel, and a spinelliferous rim along contacts with ilmenite is common (Fig. 2E, F). The presence of spinel within ilmenite lamellae (Fig. 2E) indicates that a certain amount of spinel was exolved simultaneously with ilmenite. Ti-magnetite often occurs as small grains at the ends of larger ilmenites and is therefore later in the crystallization sequence.

Two main types of mineralization in the ultramafic rocks, disseminated and net-textured (without any massive type), have been observed in QMUI (Fig. 2B–D). According to *Kärkkäinen* et al. (1997) the QMUI is considered a low grade (4–9 wt.% TiO_2) titanium deposit.

Sulfide minerals (totally <3 vol.%), with pyrrhotite as the main mineral, occurs in three generations; i.e. interstitial, inclusions (droplets) in other minerals, and late stage veinlets often associated with magnetite. Based on textural features, olivine and apatite crystallized early, followed by clinopyroxene, ilmenite, Ti-magnetite, spinel and sulfides.

Mafic rocks

The mafic rocks generally have a simple mineral assemblage (clinopyroxene, plagioclase and ilmenite). Texturally these rocks include granular, coarse- to medium-grained gabbro, microgabbro, foliated gabbro and amphibolite with irregular to gradational transitions. Amphibolites, based on field and petrographic observations, are derived from both coarse-grained and microgabbros in local shear zones, and are mainly composed of plagioclase, hornblende and ilmenite-rich bands (orthoamphibolite). Granular gabbros, the main mafic rocks, contain plagioclase (42–78 vol.%), clinopyroxene (2–42 vol.%) and ilmenite (0.5–7.2 vol.%), whereas microgabbros are usually richer in clinopyroxene (22–52 vol.%). Plagioclase is unzoned and clinopyroxene mostly contains exsolved ilmenite in two crystallographic directions. All of the mafic rocks exclusively contain ilmenite as the only Fe-Ti oxide. Magnetite, olivine and apatite, are not present, even in trace amounts. Uralitization and saussuritization of clinopyroxene and plagioclase are common.

Mineral compositions

Olivine

Average olivine core compositions vary between Fo_{63} and $Fo_{42.5}$ (Table 2). The apatite-poor, oxide-rich dunites have Mg-richer olivine ($\sim Fo_{60–63}$) than apatite-rich samples ($\sim Fo_{40–58}$; Fig. 3A). However, rims are 2–6% richer in Fo when olivine is in contact with oxides (Fig. 4A), what probably reflects re-equilibration rather than the primary composition. The MnO content varies between 0.4 and 0.8 wt.% and is negatively correlated with Mg#, which is probably related to fractional crystallization processes. The CaO content is lower than 0.05 wt.% and not correlated with other elements. There is a relatively systematic change in Fo from ~47 to 62 and from ~42 to 58 at the MZI and MZII, respectively. Al_2O_3, Cr_2O_3, NiO and TiO_2 contents in olivine mostly are low or even below detection limits (<0.01 wt.%).

Clinopyroxene

Clinopyroxene core compositions in ultramafic and mafic rocks range from $Wo_{41.58}$ $En_{36.30}$ $Fs_{12.16}$ to $Wo_{47.94}$ $En_{40.31}$ $Fs_{21.86}$ (diopside to magnesium-rich augite, according to *Morimoto*, 1989) and Mg# varies from ~64 to 76 (Table 3). The Al_2O_3 and MnO are 3.7–5.7 wt.% and 0.19–0.43 wt.%, respectively. The TiO_2 content of clinopyroxene is relatively high, up to 1.47 wt.%. Most clinopyroxene grains are unzoned (Fig. 4B). There are no major compositional differences or any systematic variation in clinopyroxene from the gabbros and ultramafic rocks (Fig. 5A).

Plagioclase

Average plagioclase core compositions in ultramafic rocks and coarse-grained gabbros are in the relatively limited range of An_{45} to An_{52} (Table 4). Plagioclase in

Table 2. *Representative microprobe analyses of olivine cores (average), standard deviation within brackets*

Rock type	ox-ub		ap-ox-ub				
Sample no.	TM62	TM16	TM17	TM61	TM134	TM138	TM147
No. of crystals	$n=6$	$n=9$	$n=7$	$n=7$	$n=7$	$n=6$	$n=5$
Mineral	Ol	Ol	Ol	Ol	Ol	Ol	Ol
SiO_2 (wt.%)	35.91 (0.23)	35.84 (0.16)	35.09 (0.22)	34.40 (0.13)	34.68 (0.20)	34.37 (0.16)	33.79 (0.14)
TiO_2	0.01 (0.01)	0.02 (0.04)	0.02 (0.02)	0.01 (0.01)	0.02 (0.02)	0.02 (0.02)	0.03 (0.06)
Al_2O_3	0.00 (0.00)	0.01 (0.01)	0.00 (0.00)	0.01 (0.01)	0.01 (0.01)	0.01 (0.01)	0.01 (0.01)
Cr_2O_3	0.01 (0.01)	0.00 (0.01)	0.02 (0.02)	0.00 (0.00)	0.00 (0.00)	0.00 (0.00)	0.01 (0.01)
FeO	33.06 (0.44)	33.99 (0.39)	36.45 (0.44)	38.27 (1.31)	40.01 (0.70)	40.25 (0.31)	41.95 (0.34)
MnO	0.41 (0.06)	0.47 (0.03)	0.56 (0.05)	0.66 (0.03)	0.65 (0.03)	0.63 (0.05)	0.67 (0.04)
NiO	0.02 (0.04)	0.02 (0.01)	0.02 (0.03)	0.37 (0.79)	0.02 (0.03)	0.03 (0.03)	0.03 (0.03)
MgO	31.26 (0.13)	30.38 (0.15)	27.88 (0.20)	25.15 (0.12)	25.58 (0.36)	25.15 (0.28)	23.37 (0.24)
CaO	0.02 (0.00)	0.02 (0.02)	0.03 (0.01)	0.03 (0.01)	0.04 (0.02)	0.01 (0.01)	0.02 (0.01)
Na_2O	0.00 (0.01)	0.00 (0.01)	0.01 (0.01)	0.01 (0.00)	0.01 (0.01)	0.00 (0.01)	0.01 (0.01)
K_2O	0.00 (0.00)	0.01 (0.01)	0.00 (0.00)	0.01 (0.00)	0.00 (0.01)	0.00 (0.00)	0.00 (0.00)
Total	100.71	100.76	100.09	98.90	101.02	100.48	99.89
Structural formula based on 4O							
Si	0.981	0.983	0.983	0.989	0.980	0.978	0.978
Ti	0.000	0.000	0.000	0.000	0.000	0.000	0.001
Al	0.000	0.000	0.000	0.000	0.000	0.000	0.000
Cr	0.000	0.000	0.000	0.000	0.000	0.000	0.000
Fe^{2+}	0.755	0.779	0.854	0.919	0.945	0.958	1.016
Mn	0.009	0.011	0.013	0.016	0.015	0.015	0.016
Ni	0.000	0.000	0.000	0.008	0.001	0.001	0.001
Mg	1.272	1.242	1.164	1.077	1.077	1.067	1.009
Ca	0.001	0.001	0.001	0.001	0.001	0.000	0.001
Na	0.000	0.000	0.000	0.000	0.000	0.000	0.000
K	0.000	0.000	0.000	0.000	0.000	0.000	0.000
Σ *cations*	3.019	3.017	3.020	3.011	3.020	3.021	3.021
Mg#	62.76 (0.40)	61.43 (0.37)	57.69 (0.43)	53.96 (0.85)	53.27 (0.76)	52.69 (0.43)	49.83 (0.42)

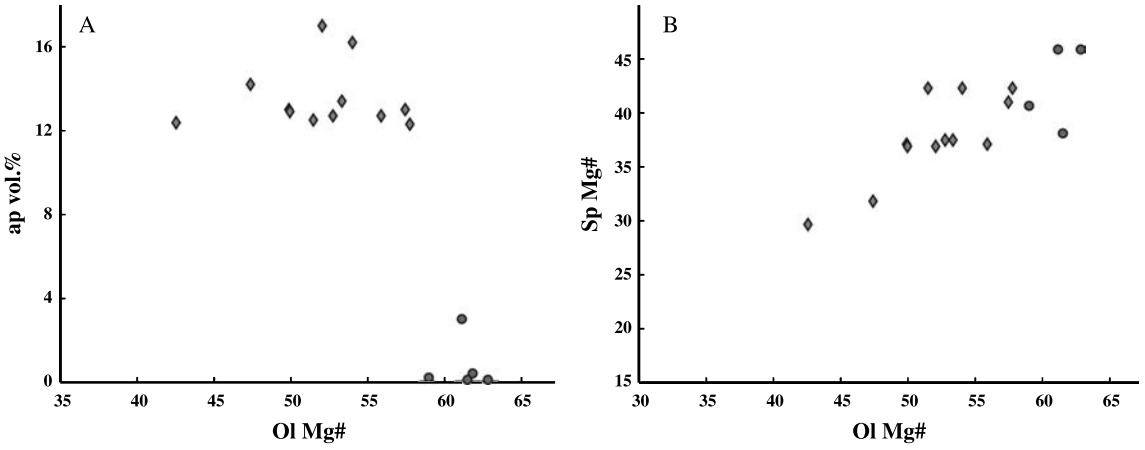

Fig. 3. (A) Plot of apatite vol.% vs. olivine Mg-number; (B) Plot of olivine Mg-number vs. spinel Mg-number in the FTP (apatite-poor samples, solid circles; apatite-rich samples, solid diamonds) of the QMUI

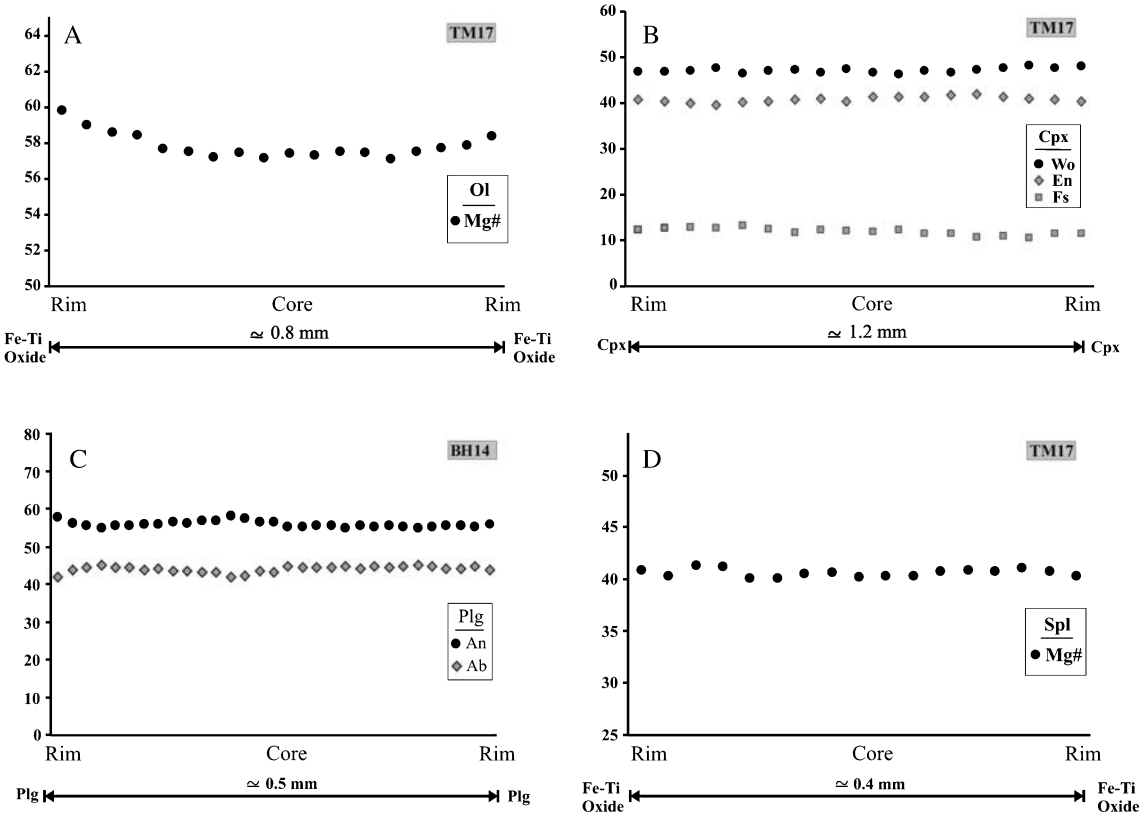

Fig. 4. Representative zoning profiles through olivine (A), clinopyroxene (B), plagioclase (C) and spinel (D) grains from samples of the QMUI. *Wo* wollastonite; *En* enstatite; *Fs* ferrosilite; *An* anorthite; *Ab* albite

microgabbro has the most An-rich composition ($An_{57–60}$), without significant zoning (Fig. 4C) and amphibolites derived from these rocks have plagioclase with about 47% An. More than 90% of the plagioclases analyzed have An_{47}–An_{50}.

Table 3. *Representative microprobe analyses of clinopyroxene (cpx), amphibole (amph) and spinel (sp) in different rocks from QMUI*

Rock type	mgb	cgb		ox-ub	ap-ox-ub				ampb	ap-ox-ub	ox-ub	ap-ox-ub		
Sample no.	BH14	TM18	TM48	TM62	TM147	TM65	TM134	TM17	TM181	TM138	TM62	TM17	TM65	TM134
Mineral	cpx	cpx	cpx	cpx	cpx	cpx	cpx	cpx	amph	amph	sp	sp	sp	sp
SiO_2 (wt.%)	48.79	48.97	49.88	48.99	50.10	49.57	48.88	49.91	43.57	39.82	0.09	0.02	0.06	0.02
TiO_2	0.92	1.22	0.75	1.40	0.93	1.24	1.05	1.20	1.12	3.61	0.11	0.05	0.10	0.09
Al_2O_3	4.79	5.25	4.47	5.66	3.92	4.56	4.52	4.47	10.39	13.77	57.60	59.51	57.56	57.56
Cr_2O_3	0.04	0.00	0.00	0.00	0.03	0.00	0.01	0.01	0.02	0.01	0.21	0.26	0.09	0.13
Fe_2O_3									4.60	2.43	6.16	3.34	5.68	5.38
FeO	10.86	9.45	10.35	8.72	11.64	9.63	10.98	7.48	12.22	10.59	23.48	24.89	25.47	26.88
MnO	0.24	0.28	0.29	0.20	0.37	0.21	0.30	0.19	0.21	0.14	0.22	0.22	0.24	0.19
NiO	0.06	0.02	0.00	0.03	0.00	0.00	0.00	0.00	10.68	11.86	0.01	0.07	0.00	0.08
MgO	12.32	12.93	12.67	13.89	12.63	12.98	12.80	13.98	0.00	0.20	11.31	10.22	9.82	8.86
CaO	20.62	20.61	20.15	20.12	19.68	20.66	19.85	21.30	11.69	11.55	0.00	0.02	0.00	0.00
Na_2O	0.70	0.64	0.50	0.63	0.66	0.63	0.64	0.79	1.29	2.97	0.00	0.04	0.05	0.05
K_2O	0.01	0.00	0.07	0.02	0.00	0.00	0.00	0.02	0.71	0.65	0.00	0.00	0.00	0.00
Total	99.35	99.37	99.11	99.66	99.95	99.49	99.01	99.35	96.50	97.59	99.18	98.64	99.06	99.24
Cations														
Si	1.853	1.846	1.886	1.832	1.889	1.866	1.859	1.867	6.552	5.922	0.003	0.000	0.002	0.001
Ti	0.026	0.035	0.021	0.039	0.026	0.035	0.030	0.034	1.841	2.413	0.002	0.001	0.002	0.002
Al	0.214	0.233	0.199	0.249	0.174	0.202	0.203	0.197	0.126	0.404	1.859	1.925	1.875	1.883
Cr	0.001	0.000	0.000	0.000	0.001	0.000	0.000	0.000	0.002	0.001	0.005	0.006	0.002	0.003
Fe^{3+}	0.000	0.000	0.000	0.000	0.000	0.000	0.000	0.000	0.521	0.272	0.127	0.069	0.118	0.112
Fe^{2+}	0.345	0.298	0.327	0.273	0.367	0.303	0.349	0.234	1.536	1.317	0.538	0.571	0.589	0.624
Mn	0.008	0.009	0.009	0.006	0.012	0.007	0.010	0.006	0.027	0.018	0.005	0.005	0.006	0.005
Ni	0.002	0.001	0.000	0.001	0.000	0.000	0.000	0.000	0.000	2.629	0.000	0.001	0.000	0.002
Mg	0.698	0.726	0.714	0.774	0.710	0.728	0.726	0.779	2.394	0.024	0.462	0.418	0.404	0.367
Ca	0.839	0.832	0.816	0.806	0.795	0.833	0.809	0.854	1.884	1.841	0.000	0.001	0.000	0.000
Na	0.052	0.046	0.037	0.046	0.048	0.046	0.047	0.058	0.376	0.856	0.000	0.002	0.002	0.003
K	0.000	0.000	0.003	0.001	0.000	0.000	0.000	0.001	0.137	0.124	0.000	0.000	0.000	0.000
Σ *cations*	4.038	4.026	4.013	4.028	4.022	4.021	4.033	4.030	15.396	15.821	3.000	3.000	3.000	3.000
No. of O	6	6	6	6	6	6	6	6	23	23	4	4	4	4
Wo	44.60	44.83	43.94	43.50	42.49	44.68	42.94	44.60						
En	37.08	39.12	38.45	41.79	37.92	39.06	38.53	37.08						
Fs	18.33	16.04	17.61	14.71	19.59	16.25	18.54	18.33						
Mg#	66.9	70.9	68.6	74.0	66.0	70.6	67.5	76.90	60.92	66.62	46.20	42.30	40.70	37.00

ampb Amphibolite, other abbreviations are explained in Table 1

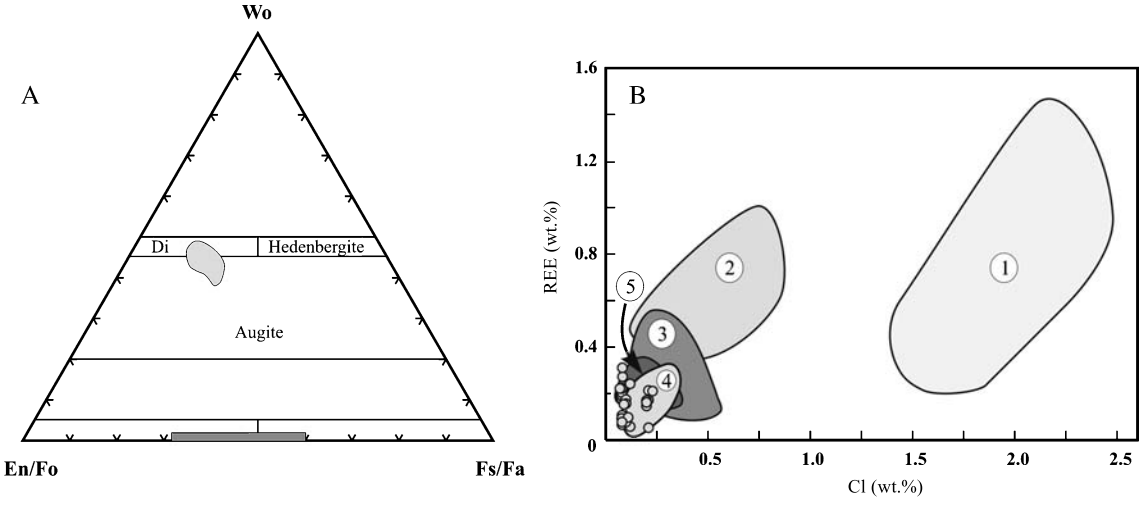

Fig. 5. (A) Compositional range of clinopyroxene and olivine in gabbros and FTP rocks from QMUI. (B) Plot of Cl content versus REE (Ce + La + Nd) abundances of apatite in the QMUI (solid circles) and other localities. *1* Mantle apatite A (data from *O'Reilly* and *Griffin*, 2000; Table 1); *2* Babbitt massive Cu–Ni mineralization (data from *Ripley* et al., 1998); *3* mantle apatite B (data from *O'Reilly* and *Griffin*, 2000; Table 2); *4* Boulder lake apatite-rich oxide ultramafic intrusions (data from *Ripley* et al., 1998); *5* oxide-apatite gabbronorite (data from *Dymek* and *Owens*, 2001; Table 4)

Apatite

All apatites are fluor-apatite (Table 5) and contain high F contents (~ 2 wt.%) and low Cl (≤ 0.2 wt.%), which is consistent with a high-temperature magmatic origin. Most of the apatites have relatively homogenous major element compositions. P_2O_5 and CaO contents (in wt.%) vary from ~ 43 to 44 and ~ 54 to 55, respectively and concentrations of Na_2O, MnO, FeO and MgO are low (≤ 0.1 wt.%). Molar Cl/F ratios tend to be consistent with values of 0.02–0.04. REE (Ce + La + Nd) concentrations in apatites are 1600–3200 ppm. The low Cl- and REE contents (La + Ce + Nd) of apatites in QMUI are much closer to those of type B (magmatic crystallization product) than type A (metasomatic product) mantle apatites (Fig. 5B). No obvious compositional differences between apatite inclusions in silicate minerals and large interstitial apatites were detected.

Ilmenite

Ilmenite in the mafic rocks (Table 6) is close to its end-member composition ($X_{ilm} \sim 0.96$–0.98) and shows only submicroscopic exsolutions. In these rocks, ilmenite has low MgO (≤ 0.20 wt.%) but high MnO (0.92–1.60 wt.%) contents. Ilmenite in the ultramafic rocks shows thin hematite exsolutions (hemoilmenite), and X_{ilm} range from 0.82 to 0.91. They have high MgO and low MnO when compared with ilmenite in the mafic rocks (Table 6). Apatite-poor ultramafic samples usually contain ilmenite with relatively higher MgO than apatite-rich ones (Table 6). Exsolved lamellae of ilmenite in Ti-magnetite are nearly pure ilmenite. Although

Table 4. *Representative microprobe analyses of plagioclase (average) in different rocks from QMUI, standard deviation within brackets*

Rock type	ox-ub	ap-ox-ub		cgb			mgb
Sample no.	TM62	TM142	TM147	TM18	TM54	TM48	BH14
No. of crystals	$n=5$	$n=6$	$n=4$	$n=7$	$n=5$	$n=6$	$n=8$
SiO_2 (wt.%)	54.43 (0.32)	55.48 (0.12)	55.38 (0.67)	54.77 (0.13)	55.25 (0.31)	55.81 (0.14)	53.61 (0.23)
Al_2O_3	28.67 (0.11)	28.81 (0.13)	27.97 (0.29)	28.45 (0.08)	28.38 (0.30)	28.03 (0.14)	29.79 (0.12)
FeO	0.06 (0.03)	0.07 (0.02)	0.05 (0.01)	0.09 (0.02)	0.11 (0.04)	0.08 (0.03)	0.07 (0.03)
CaO	10.58 (0.05)	9.25 (0.14)	9.18 (0.47)	10.24 (0.12)	9.80 (0.23)	9.48 (0.11)	11.36 (0.21)
Na_2O	5.24 (0.11)	4.98 (0.36)	6.22 (0.12)	5.58 (0.11)	5.66 (0.13)	5.87 (0.09)	4.03 (0.15)
K_2O	0.12 (0.01)	0.08 (0.01)	0.09 (0.02)	0.25 (0.04)	0.16 (0.04)	0.16 (0.09)	0.02 (0.01)
Total	99.10 (0.49)	98.66 (0.18)	98.90 (0.03)	99.38 (0.07)	99.35 (0.14)	99.43 (0.22)	98.88 (0.20)
Structural formula based on 8O							
Si	2.47	2.51	2.51	2.52	2.50	2.52	2.44
Al	1.54	1.54	1.50	1.49	1.51	1.49	1.60
Fe	0.00	0.00	0.00	0.00	0.00	0.00	0.00
Ca	0.51	0.45	0.45	0.46	0.47	0.46	0.55
Na	0.46	0.44	0.55	0.52	0.50	0.51	0.35
K	0.01	0.00	0.01	0.01	0.01	0.01	0.00
Σ *cations*	4.97	4.94	5.01	5.00	5.00	4.99	4.94
An	0.52 (0.01)	0.50 (0.02)	0.45 (0.02)	0.47 (0.02)	0.48 (0.01)	0.47 (0.01)	0.61 (0.01)
Ab	0.47 (0.01)	0.49 (0.02)	0.55 (0.02)	0.52 (0.02)	0.51 (0.01)	0.52 (0.00)	0.39 (0.01)
Or	0.01 (0.00)	0.00 (0.00)	0.01 (0.00)	0.01 (0.00)	0.01 (0.00)	0.01 (0.01)	0.00 (0.00)

the variations in both Mg and Mn in ilmenite are not entirely systematic, the overall trend appears to be real and may reflect control by fractional crystallization. There is a small compositional difference between ilmenite droplets and large interstitial ilmenite grains. Hematite lamellae in ilmenite show higher TiO_2 and are Ti-hematite in composition ($X_{ilm} \sim 0.26$–0.30, Table 6).

Magnetite (Ti-magnetite)

Most magnetite grains contain intergrowths of both ilmenite and hercynitic spinel. Bulk composition of these grains was determined by analysis with a defocused beam of 40 μm size. Most magnetites have low X_{usp} component (0.03–0.13) and therefore high X_{mag} component (0.79–0.93, Table 6). The MgO and MnO contents vary from 0.58 to 1.38 wt.% and up to 0.08 wt.%, respectively. However, no systematic variation in magnetite composition has been observed with respect to the stratigraphic level in the ultramafic rock sequence. The Cr_2O_3 concentrations are low (≤ 0.22 wt.%) but V_2O_5 contents are high (0.93–1.90 wt.%). Magnetite in the late stage veinlets has end-member magnetite composition ($X_{mag} \sim 0.998$). Al_2O_3 content is high, but variable (1.21–3.53 wt.%) because of the inhomogeneous distribution of hercynitc spinel exsolutions.

Table 5. *Representative microprobe analyses of apatite cores (average) in FTP from QMUI, standard deviation within brackets*

Rock type	ap-ox-ub					
Sample no. No. of crystals	TM65 $n=7$	TM138 $n=8$	TM17 $n=6$	TM147 $n=6$	TM139 (core)	TM139 (rim)
P_2O_5 (wt.%)	42.99 (0.48)	42.88 (0.16)	43.38 (0.12)	42.62 (0.18)	43.30	43.16
SiO_2	0.12 (0.03)	0.09 (0.02)	0.10 (0.01)	0.10 (0.01)	0.10	0.11
FeO	0.11 (0.09)	0.12 (0.04)	0.00 (0.00)	0.10 (0.04)	0.00	0.00
CaO	54.48 (0.12)	54.07 (0.06)	54.37 (0.07)	53.56 (0.02)	55.28	55.19
MnO	0.03 (0.00)	0.03 (0.02)	0.02 (0.02)	0.03 (0.05)	0.01	0.04
MgO	0.04 (0.01)	0.06 (0.01)	0.01 (0.01)	0.03 (0.01)	0.05	0.03
SrO	0.00 (0.00)	0.00 (0.00)	0.00 (0.00)	0.01 (0.01)	0.00	0.00
Na_2O	0.04 (0.02)	0.07 (0.01)	0.02 (0.00)	0.04 (0.02)	0.04	0.04
H_2O	0.81 (0.00)	0.78 (0.02)	0.77 (0.01)	0.76 (0.02)	0.84	0.84
F	2.03 (0.04)	2.09 (0.04)	2.07 (0.02)	2.09 (0.06)	2.00	1.99
Cl	0.10 (0.02)	0.08 (0.01)	0.21 (0.01)	0.08 (0.01)	0.10	0.09
Total	100.74	100.28	100.95	99.42	101.7	101.49
O=F, Cl	0.85 (0.01)	0.91 (0.02)	0.92 (0.01)	0.91 (0.02)	0.86	0.86
Total	99.89	99.37	100.30	98.51	100.84	100.63
La (ppm)	270 (130)	340 (95)	290 (100)	370 (130)	n.d.	n.d.
Ce	730 (330)	878 (233)	780 (260)	960 (340)	n.d.	n.d.
Nd	560 (210)	682 (139)	620 (180)	750 (230)	n.d.	n.d.

n.d. Not detected

Accessory minerals

The PROBE-AMBH program (*Tindle* and *Webbe*, 1994) was used for the classification and calculation of site occupation of amphiboles. The amphiboles (as reaction rims) in the ultramafic rocks and gabbros commonly are titanian-ferroan-pargasite and titanian-magnesian-hastingsite with relatively high TiO_2 contents (1.12–3.61 wt.%; Table 3). Amphibole in amphibolite is magnesio-hornblende. Furthermore, secondary actinolite/actinolitic hornblende was detected in various rocks of QMUI and probably formed during a later alteration stage.

All spinels in ultramafic rocks are hercynitic spinel, without significant zoning (Fig. 4D), and the chemical composition (in wt.%) varies in the range 57–60 for Al_2O_3, 7.0–11.3 for MgO, 28.7–32.3 for FeO with very low contents of Cr_2O_3 (≤ 0.26 wt.%). There is a positive correlation between Mg content of olivine, spinel and Fe-Ti oxides (Tables 2, 3 and 6). Spinel in apatite-poor ultramafic samples shows high Mg-numbers (~ 43–46) when compared with apatite-rich ones (~ 30–44; Table 3, Fig. 3B). The Cr-number always is very low (≤ 0.003) and TiO_2 content is up to 0.15 wt.%.

Pyrrhotite is the main sulfide mineral in ultramafic rocks and microgabbros, and usually encloses chalcopyrite and rarely pentlandite. Pyrrhotite has a low content of Ni (<0.20 wt.%) and Co (<0.16 wt.%).

Table 6. *Representative microprobe analyses of ilmenite (ilm), magnetite (mag), hematite exsolution (hem-ex) and magnetite in veinlets (mag-v) in different rocks from QMUI.* $X_{hem} = 0.5 \times Fe^{3+}$, $X_{Gk} = N_{Mg}$, $XPy = N_{Mn}$, $X_{ilm} = 1 - (X_{hem} + X_{Gk} + X_{Py})$, $X_{mag} = 0.5 \times Fe^{3+}$, $X_{usp} = N_{Ti}$, *other abbreviations are explained in Table 1*

Rock type	mgb	cgb	ox-ub	ap-ox-ub						ox-ub	ap-ox-ub					ox-ub
Sample no.	BH14	TM18	TM62	TM65	TM134	TM61	TM27	TM147	TM138	TM62	TM65	TM134	TM61	TM27	TM147	TM13
Mineral	ilm	ilm	ilm	ilm	ilm	ilm	ilm	ilm	hem-ex	mag	mag	mag	mag	mag	mag	mag-v
SiO_2	0.03	0.00	0.00	0.07	0.02	0.03	0.03	0.05	0.03	0.03	0.05	0.05	0.03	0.18	0.08	
TiO_2	53.17	52.99	49.81	51.01	50.11	51.18	50.34	50.21	16.99	3.98	4.61	1.50	3.19	1.37	0.99	0.052
Al_2O_3	0.03	0.04	0.01	1.28	0.02	0.02	0.03	0.03	2.07	2.75	2.23	2.42	3.53	3.39	1.21	0.017
Cr_2O_3										0.22	0.07	0.09	0.00	0.12	0.11	0
FeO	45.71	45.18	48.07	45.14	46.94	46.31	48.33	47.58	77.82	84.23	84.16	87.87	84.81	85.44	89.77	92.334
MnO	1.03	0.92	0.58	0.74	0.93	0.86	0.92	0.88	0.27	0.04	0.08	0.05	0.08	0.04	0.05	0.022
MgO	0.17	0.19	2.38	1.39	1.00	1.09	0.82	0.89	1.49	0.83	0.58	0.65	0.77	1.38	0.60	0.09
CaO	0.09	0.00	0.01	0.00	0.03	0.10	0.00	0.00	0.03							
ZnO										0.07	0.121	0.03	0.12	0.07	0.09	
V_2O_3										1.899	1.074	0.95	0.931	1.899	0.942	
Total	100.22	99.32	100.86	99.63	99.05	99.59	100.47	99.63	98.69	94.04	92.96	93.61	93.46	93.89	93.82	92.515
Cations																
Si	0.001	0.000	0.000	0.002	0.000	0.001	0.001	0.001	0.001	0.001	0.002	0.002	0.001	0.007	0.003	0.000
Ti	1.004	1.008	0.917	0.954	0.950	0.966	0.942	0.948	0.309	0.113	0.132	0.043	0.090	0.039	0.028	0.002
Al	0.001	0.001	0.000	0.037	0.001	0.000	0.001	0.001	0.059	0.122	0.100	0.108	0.157	0.149	0.054	0.001
Cr	0.000	0.000	0.000	0.000	0.000	0.000	0.000	0.000	0.000	0.007	0.002	0.003	0.000	0.004	0.003	0.000
Fe^{3+}	0.000	0.000	0.166	0.050	0.098	0.067	0.113	0.102	1.323	1.586	1.596	1.772	1.632	1.700	1.852	1.996
Fe^{2+}	0.960	0.956	0.818	0.889	0.893	0.904	0.893	0.897	0.249	1.064	1.095	1.005	1.042	0.965	0.993	0.996
Mn	0.022	0.020	0.012	0.015	0.020	0.018	0.019	0.019	0.006	0.001	0.002	0.001	0.002	0.001	0.001	0.001
Ni	0.000	0.000	0.000	0.000	0.000	0.000	0.000	0.000	0.000	0.000	0.000	0.000	0.000	0.000	0.000	0.000
Mg	0.006	0.007	0.087	0.052	0.038	0.041	0.030	0.033	0.054	0.046	0.033	0.037	0.044	0.077	0.034	0.005
Ca	0.002	0.000	0.000	0.000	0.001	0.003	0.000	0.000	0.001	0.000	0.000	0.000	0.000	0.000	0.000	0.000
Na	0.000	0.000	0.000	0.000	0.000	0.000	0.000	0.000	0.000	0.000	0.000	0.000	0.000	0.000	0.000	0.000
K	0.000	0.000	0.000	0.000	0.000	0.000	0.000	0.000	0.000	0.000	0.000	0.000	0.000	0.000	0.000	0.000
Zn										0.002	0.003	0.001	0.003	0.002	0.002	
V										0.057	0.033	0.029	0.028	0.057	0.029	
Σ *cations*	1.995	1.992	2.000	2.000	2.000	1.998	2.000	2.000	2.000	3.000	3.000	3.000	3.000	3.000	3.000	3.000
No. of O	3	3	3	3	3	3	3	3	3	4	4	4	4	4	4	4
X_{ilm}/X_{mag}	0.972	0.973	0.818	0.908	0.894	0.907	0.894	0.897	0.279	0.793	0.798	0.886	0.816	0.850	0.926	0.998
X_{hem}/X_{usp}	0.000	0.000	0.083	0.025	0.049	0.034	0.056	0.051	0.661	0.113	0.132	0.043	0.090	0.039	0.028	0.002
X_{Gk}	0.006	0.007	0.087	0.052	0.038	0.041	0.030	0.033	0.054							
X_{py}	0.022	0.020	0.012	0.015	0.020	0.018	0.019	0.019	0.006							

Estimates of crystallization conditions and post crystallization processes

Crystallization temperature estimates, using the clinopyroxene-ilmenite geothermometer (*Bishop*, 1980), yield subsolidus equilibration temperatures from 777 to 1028 °C for the ultramafic rocks. There is no suitable mineral phase or assemblage for direct calculation of pressure; hence, a pressure of 2 kbar was assumed for the calculations. The clinopyroxene geothermometer (*Kretz*, 1994), on the basis of core compositions, yields 936–1004 °C for the ultramafic rocks and from 942 to 948 °C for gabbros. The two oxide geothermobarometer (*Andersen* and *Lindsley*, 1985) in the ILMAT program (*Lepage*, 2003) results in re-equilibration temperatures (450–700 °C) and oxygen fugacities (around 10^{-19} fO_2) for the ultramafic rocks. It is assumed that magnetite re-equilibrates by intraoxide reaction (*Buddington* and *Lindsley*, 1964) in which the ulvöspinel component of magnetite-ulvöspinel solid solution oxidizes and produces lamellae and granules of ilmenite within or around magnetite at intermediate temperatures. Hence, in this study, bulk compositions of thin ilmenite exsolution-bearing titanomagnetite and fine and submicroscopic hematite bearing-ilmenite were obtained by using data obtained with a defocused beam of 40 μm. In addition to Fe and Ti diffusion between oxides during cooling, post-magmatic Fe-Mg diffusion affecting olivine and clinopyroxene can result in Mg decrease in both ilmenite and magnetite when they are in contact with these silicate phases (*Frost* and *Lindsley*, 1992). This explains why the silicates, in particular olivine, that are in contact with oxides show higher Mg contents in the rims (Fig. 4A).

Whole-rock geochemistry

Fifty samples of QMUI were analyzed for major and trace elements (including REE) and results of 16 representative samples are listed in Table 7.

Major elements

In Bowen diagrams (Fig. 6) many oxides display good correlations with MgO, except for phosphorus and CaO (not plotted) which scatter over the whole range of MgO. Al_2O_3, total alkalis and SiO_2 are negatively correlated with MgO while MnO, $Fe_2O_3^{tot}$ and TiO_2 show positive correlation. In most diagrams (Fig. 6), the ultramafic and mafic rocks form two separated clusters and there is a compositional gap between them reflecting distinct differences in their modal compositions (Table 1). Ultramafic rocks are enriched in Fe ($Fe_2O_3^{tot}$: 26–42 wt.%), TiO_2 (5–11 wt.%), P_2O_5 (up to 5.1 wt.%) and X_{Fe} ($Fe_2O_3^{tot}/Fe_2O_3^{tot} + MgO$: 0.68–0.78) what reflects modal enrichment of ilmenite, magnetite and apatite (Table 1). These rocks have very low SiO_2 (~ 21–30 wt.%) and K_2O (0.01–0.49 wt.%) while MgO contents are high (8.8–19.8 wt.%). Some hybrid ultramafic rocks, which show mixing with xenocrysts/xenoliths of gabbros (e.g., BH34) commonly plot between the ultramafic and mafic rocks (Fig. 6). The major-element compositions, except for P_2O_5, of the ultramafic rocks from all zones are similar. Small variations in bulk compositions mostly are due to variations in modal mineralogy (Table 1) and to a lesser degree in mineral compositions (Tables 2–6). The difference in P_2O_5 content is the most noticeable feature of the ultramafic part of QMUI. The high MgO and

Table 7. *Representative whole-rock elemental analyses of different rock types from QMUI. Major oxides in wt.% and trace elements and REE in ppm. Four FTP samples from other localities are included for comparison. 1 Duluth complex, Boulder lake area, oxide-apatite dunite (*Ripley *et al., 1998; Table 2); 2 Bushveld complex, Upper Zone, Villa Nora area, olivine-apatite-oxide rock (*Von Gruenewaldt, *1993; Table 3); 3 Roseland anorthosite, Virginia, oxide-apatite gabbronorite "OAGN" (*Dymek *and* Owens, *2001; Table 2); 4 Kauhajärvi gabbro, Finland, peridotite (*Kärkkaäinen *and* Appelqvist, *1999; Table 1)*

Rock type	ox-ub		ap-ox-ub							
Sample no.	TM16	TM62	TM17	TM27	TM46	TM61	TM65	TM134	TM138	TM140
SiO_2	27.4	30.7	25.1	25.3	26	22.1	24	25.4	22.6	22.2
TiO_2	10.55	11.1	7.7	8.29	7.87	8.52	8.78	8.16	7.82	7.45
Al_2O_3	2.11	5.96	1.89	1.47	1.85	1.04	1.3	1.59	1.1	1.51
$Fe_2O_3^{tot}$	39.1	31.1	37.7	38	35.5	40.4	38.8	38.3	40	39.9
MnO	0.42	0.34	0.42	0.49	0.46	0.43	0.42	0.46	0.46	0.43
MgO	18.45	13.5	14.75	13.05	13.15	13.85	15.1	13.3	15.6	14.45
CaO	1.33	5.34	8.21	8.45	9.89	6.98	6.86	8.4	6.27	7.95
Na_2O	0.14	0.89	0.13	0.18	0.15	0.08	0.1	0.13	0.12	0.12
K_2O	0.04	0.9	0.01	0.03	0.02	0.02	0.02	0.02	0.03	0.03
P_2O_5	0.07	0.09	3.97	4.05	4.25	4.6	3.81	3.94	3.93	4.89
Ba	18.3	37.6	20	27.8	11.7	11.6	8.6	12.2	10.6	10.4
Nb	27	28	14	27	18	24	21	18	24	23
Rb	0.7	0.7	0.3	0.7	0.3	0.7	0.5	0.4	0.5	0.6
Cs	0.1	<0.1	0.1	<0.1	0.1	<0.1	<0.1	0.1	0.1	0.1
Sr	22.3	154	85.4	85.7	85.6	92.1	74.7	77.6	73.4	99.4
Y	2.2	6.1	41.5	47.8	42.6	55	36.9	45.4	40.7	53.1
Zr	41.1	40.9	32.1	50.6	38.2	40.5	35.7	41.6	40.8	39.4
V	653	858	808	495	500	547	588	612	444	298
Cr	140	80	90	60	70	60	70	80	50	60
Ni	12	29	7	15	19	8	9	52	46	48
Co	93.1	89.2	81.9	71.5	61.7	75.6	83.8	65.5	100	97.3
Zn	281	241	268	249	244	271	242	269	231	231
Ga	10	12	13	10	12	10	10	12	8	10
Sn	1	1	1	1	<1	1	<1	1	<1	<1
Th	<1	<1	<1	<1	<1	<1	<1	<1	<1	<1
U	<0.5	<0.5	<0.5	<0.5	<0.5	<0.5	<0.5	<0.5	<0.5	<0.5
Hf	1	1	1	1	1	1	1	1	1	1
Ta	2.3	2.5	1.2	2.1	1.5	2.1	1.9	1.6	2	1.9
W	<1	<1	1	1	1	1	<1	<1	<1	<1
La	5.5	3.8	41.2	40.7	29.4	52.9	30.3	39.1	22.9	40.4
Ce	2.5	4.8	82.4	93.3	74.6	117.5	72.1	89.1	81	107
Pr	0.3	0.7	12	13.4	11.4	16.7	10.6	12.7	12.3	16.6
Nd	1.7	3.8	62.7	68.6	59	82.6	54.1	65.2	60.4	80.5
Sm	0.4	1.2	14.8	16	14.2	19.2	13	15.9	13.8	18.3
Eu	0.2	0.5	3.1	3.5	3.2	4.2	2.9	3.5	3.3	4
Gd	0.5	1.2	13.6	15.2	13.6	18.8	12.4	15	14	18
Tb	0.1	0.2	1.8	2	1.8	2.5	1.6	2	1.9	2.5
Dy	0.4	1.2	8.3	9.8	8.6	11.6	7.9	9.6	8.7	11.2
Ho	0.1	0.2	1.6	1.8	1.6	2.1	1.4	1.8	1.5	2
Er	0.2	0.6	3.8	4.4	3.9	4.9	3.4	4.3	4	4.8

(*continued*)

Table 7 (*continued*)

Rock type	ox-ub		ap-ox-ub							
Sample no.	TM16	TM62	TM17	TM27	TM46	TM61	TM65	TM134	TM138	TM140
Tm	<0.1	0.1	0.4	0.5	0.4	0.5	0.3	0.4	0.4	0.5
Yb	0.3	0.6	2.1	2.6	2.1	2.8	1.8	2.4	2.2	2.6
Lu	<0.1	0.1	0.3	0.3	0.2	0.4	0.2	0.3	0.3	0.4
Eu/Eu^*	1.37	1.27	0.67	0.69	0.7	0.68	0.7	0.69	0.73	0.67
$(La)_N/(Sm)_N$	8.89	2.04	1.8	1.64	1.34	1.78	1.5	1.59	1.07	1.43
$(La)_N/(Yb)_N$	13.19	4.54	14.08	11.23	10.04	13.55	12.07	11.68	7.47	11.15
X_{Fe}	0.68	0.7	0.72	0.74	0.73	0.74	0.72	0.74	0.72	0.73

Rock type	ap-ox-ub	hyb	mgb	cgb		mgr	1	2	3	4
Sample no.	TM147	BH2-34	BH1-14	TM18	TM35	TM78				
SiO_2	23.1	33.5	44.9	47.4	49.2	61	24.85	14.04	39.78	32.69
TiO_2	7.65	5.25	2.13	3.14	2.41	1.2	10.8	9.96	7.86	5.13
Al_2O_3	2.16	9.73	15	20.2	20.2	15.4	1.41	1.62	8.78	7.47
$Fe_2O_3^{tot}$	37.9	26	13.15	10.2	7.7	8.06	37.05	55.68	21.72	31.01
MnO	0.46	0.36	0.15	0.11	0.09	0.11	0.52	0.55	0.24	0.35
MgO	13.55	8.8	8.05	4.21	4.2	2.38	13.5	3.39	7.77	9.5
CaO	8.16	9.87	12.25	9.4	10.3	4.83	6.24	10.61	8.37	7.79
Na_2O	0.32	1.87	2.74	3.78	3.88	3.29		0.15	1.63	0.96
K_2O	0.05	0.24	0.18	0.28	0.43	0.97	0.24	0.11	0.55	0.49
P_2O_5	4.54	3.88	0.02	0.06	0.07	0.16	2.79	7.16	3.52	2.31
Ba	19.6	113	46.5	169	198	813	8		350	260
Nb	29	22	2	8	6	12			11.5	40
Rb	0.6	1.6	1.7	2.2	5.3	22.8			1.4	
Cs	0.1	0.2	1.1	1.1	0.2	0.7			<0.4	
Sr	129.5	375	293	754	730	380	38		494	
Y	54.7	48.4	21.3	5.6	7.3	25.8	57		54.6	
Zr	51.9	33.5	25.5	21.5	21.3	193.5			74.3	
V	495	301	368	300	224	215	573		329	594
Cr	70	40	340	70	40	20			116	12
Ni	41	27	114	41	26	5			41.1	
Co	92.7	59	47.2	38.2	24.8	20.4				
Zn	249	185	94	74	60	85	225		251	
Ga	11	15	17	20	19	20			18.7	
Sn	<1	1	1	1	<1	1			<7.2	
Th	<1	<1	<1	<1	<1	8			<0.16	
U	<0.5	<0.5	<0.5	<0.5	<0.5	0.8			<0.7	
Hf	1	1	1	1	1	5			2.61	
Ta	2.3	1.6	<0.5	0.7	0.5	0.7			0.88	
W	<1	1	1	1	1	<1			<8	
La	43.6	45.6	8.9	7.3	6.7	72.2			42.5	24.7
Ce	108.5	103	6.1	7.5	7.3	143.5			110.2	61.7
Pr	17	14.6	1.2	1	1.1	14.5				9
Nd	81.1	71.4	7.7	4.6	5.4	51			86	43.6
Sm	18.2	16.4	2.7	1.2	1.5	8.6			18.9	9.04
Eu	4.5	4.3	1.1	1	1.1	1.7			3.5	2.8

(*continued*)

Table 7 (*continued*)

Rock type	ap-ox-ub	hyb	mgb	cgb		mgr	1	2	3	4
Sample no.	TM147	BH2-34	BH1-14	TM18	TM35	TM78				
Gd	18.7	15.8	3.4	1.2	1.6	7.4				8.88
Tb	2.7	2.1	0.7	0.2	0.3	1			2.18	1.19
Dy	11.8	10.2	3.7	1	1.4	5.2				6.03
Ho	2.1	1.8	0.8	0.2	0.3	1				1.04
Er	5.4	4.6	2.2	0.7	0.7	3				2.75
Tm	0.6	0.4	0.3	0.1	0.1	0.4				0.37
Yb	3	2.5	1.9	0.4	0.6	2.5			3.12	2.09
Lu	0.4	0.3	0.3	0.1	0.1	0.4			0.42	0.3
Eu/Eu^*	0.75	0.82	1.11	2.55	2.17	0.65				
$(La)_N/(Sm)_N$	1.55	1.8	2.13	3.93	2.88	5.42				
$(La)_N/(Yb)_N$	10.42	13.08	3.36	13.11	8.01	20.71				
X_{Fe}	0.74	0.75	0.62	0.71	0.65	0.77	0.73	0.94	0.74	0.77

low P_2O_5 (e.g., TM62 and TM16) contents of the samples, generally located in SZI and in the lower part of MZI suggest less fractionated magmas. In the Fe_2O_3-TiO_2 diagram (Fig. 7A) the ultramafic rocks show a roughly linear trend and plot along an array subparallel to the $Fe/Ti = 4$ line, suggesting similar ilmenite/magnetite proportions in most of the samples. Al_2O_3 and Na_2O concentrations are low in most of the ultramfic rocks (Table 7), due to the low content of feldspar, while samples enriched in Al and Na (e.g., BH34) are consistent with the presence of plagioclase as xenocrysts. The linear variation within the mafic rocks is mainly controlled by the plagioclase-clinopyroxene distribution. In most diagrams (Fig. 6) various mafic rocks (e.g., coarse-grained gabbro, microgabbro) do not plot in distinct fields. Mafic rocks are richer in SiO_2 (43–52 wt.%), Al_2O_3 (15.0–24.5 wt.%), Na_2O (1.6–4.7 wt.%) and CaO (9.5–16.0 wt.%) and poorer in $Fe_2O_3^{tot}$ (4.5–17.0 wt.%), TiO_2 (0.5–4.0 wt.%), MgO (2.0–8.0 wt.%) and P_2O_5 (0.01–0.40 wt.%) with respect to ultramafic rocks (Table 7) that reflect conspicuously low content of Fe-Ti oxides, olivine and apatite.

Trace and rare earth elements

The Cr and Ni contents are generally low in QMUI. In ultramafic rocks Cr (40–160 ppm) and Ni (7–73 ppm) are lower than those of the mafic rocks (Cr: 10–340 ppm and Ni: 11–114 ppm). The V content of the ultramafic rocks (298–858 ppm) is higher than in mafic rocks (62–198 ppm) and correlates well with TiO_2. Indeed it is the only trace element that fully discriminates mafic rocks from ultramafics. The Ti/V ratio in ultramafic and mafic rocks of QMUI is 57–150 and $\leq$91, respectively. *Owens* et al. (1993) referred to Ti/V ratios of $\geq$100 as characteristic of massif-type anorthosites. Rb (0.2–1.6 ppm) and Sr (7.8–186 ppm) of the ultramafic rocks are much lower than in the mafic ones (1.7–9.3 and 226–899 ppm, respectively). The high Sr in the mafic rocks is due to its substitution for Ca in plagioclase. In most samples Hf, Cs, W, Sn, Th and U concentrations are below detection limits ($<$0.5–1 ppm). Ga does not correlate with Al_2O_3, a feature that

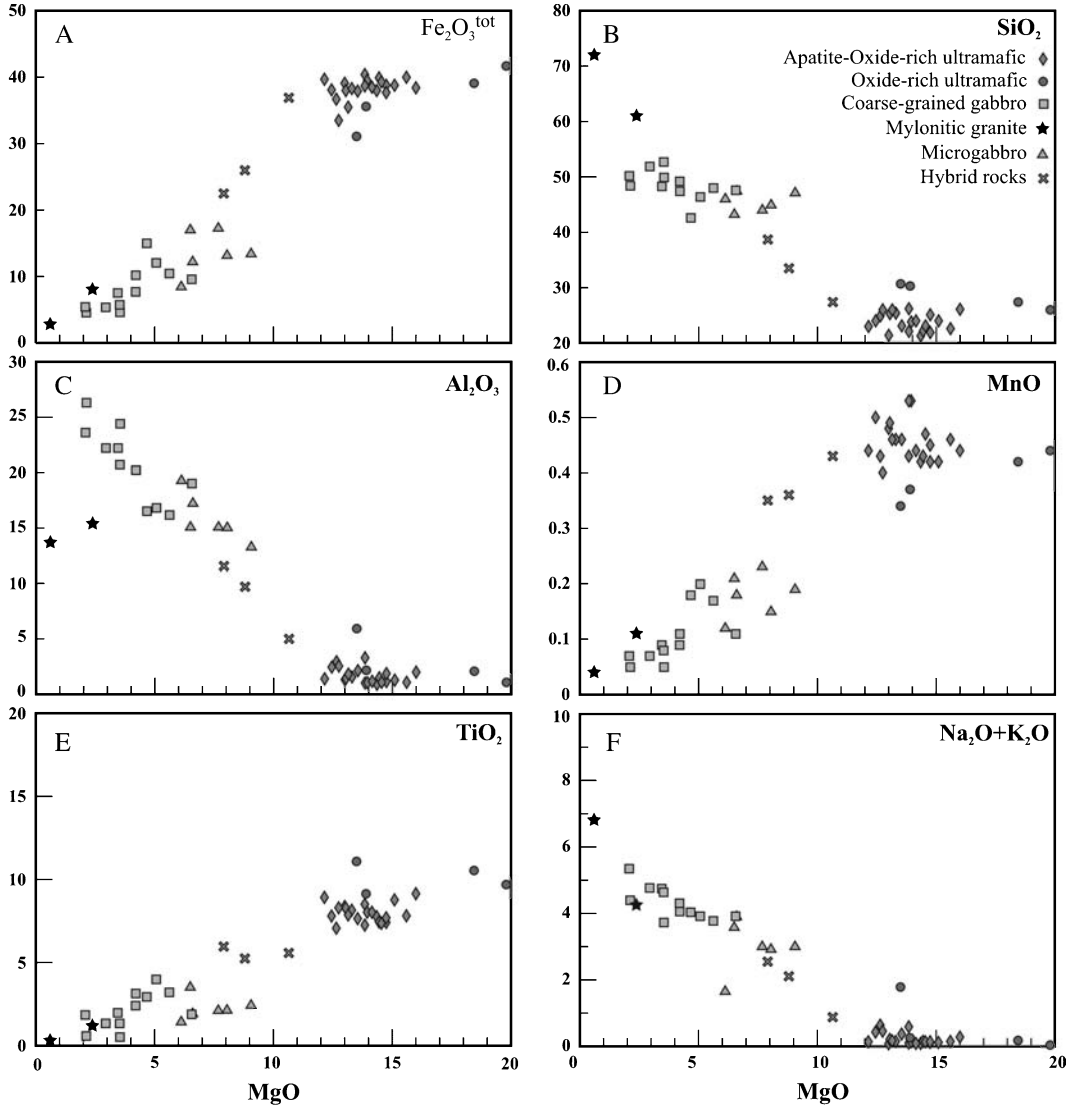

Fig. 6. Bowen diagrams for rocks of the QMUI (with all data in weight percent)

appears to characterize all rocks of the massif-type anorthosite suite (*Dymek*, 1990). Y ranges from 1.5 to 58 ppm and 2.8 to 21.3 ppm in ultramafic and mafic rocks, respectively and positively correlates with P_2O_5 in the ultramafic rocks. Zr/Hf and Nb/Ta ratios range from 29 to 57 and 11 to 14.8 for ultramafic and from 14 to 38 and 4 to 14 in the mafic rocks, respectively. The Zr/Nb ratio in the ultramafic rocks is 1.4–2.5 and in mafic rocks is 1.4–13. The contents of Y, Zr, Nb and Ta are high both in ultramafic and mafic rocks, and correlate fairly well with TiO_2 and $Fe_2O_3^{tot}$, suggesting that they are incorporated primarily in Fe-Ti oxides. Generally, microgabbros have relatively high concentration of Mg, Cr, Ni, and V when compared with the coarse-grained gabbros, indicating that clinopyroxene largely controls these elements in mafic rocks. The chondrite-normalized REE patterns of QMUI rocks are shown in Fig. 8A and B. REE patterns of aptite-rich ultramafic samples exhibit LREE enrichment ($La_N/Sm_N = 1.2–1.9$ and $La_N/Yb_N = 10–14$), and a con-

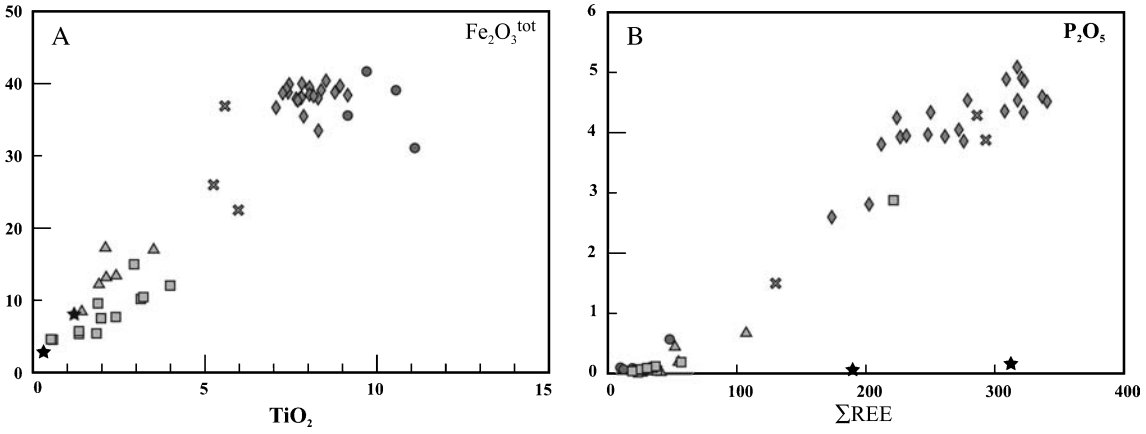

Fig. 7. (A) TiO_2 vs. $Fe_2O_3^{tot}$ (total iron) and (B) P_2O_5 vs. ΣREE (total REE) plots for various rocks of the QMUI (with REE in ppm and other data in wt.%). Symbols as in Fig. 6

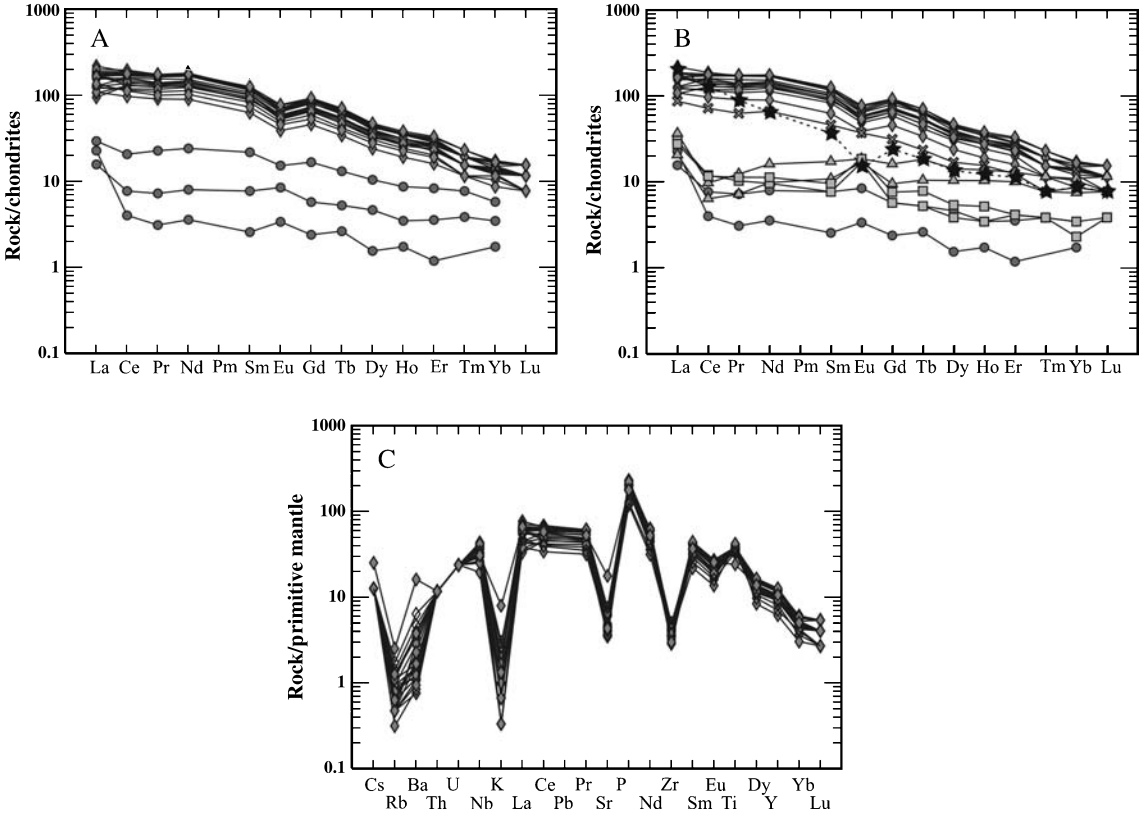

Fig. 8. Chondrite-normalized REE patterns for FTP (A) and various other rock types (B) of QMUI. Primitive mantle normalized trace element diagrams of apatite-oxide-rich ultramafic rocks (C). Symbols as in Fig. 6

cave-down shape, relatively high REE abundances (REE = 212–340 ppm) and negative Eu anomalies ($Eu/Eu^* \sim 0.7$). In most of these samples, LREEs are fractionated from Nd through Lu, although La to Nd displays low and variable slope. However,

some samples (e.g., TM138) show no or less fractionation or show a peculiar kink from La to Nd. The apatite-poor ultramafic samples (e.g., TM16), commonly have low REE abundances (REE = 10–48 ppm), show flatter patterns with weak or no Eu anomalies ($Eu/Eu^* = 0.8–1.3$) and are parallel to apatite-rich ones (Fig. 8A). Hybrid ultramafic samples show intermediate patterns between the apatite-rich rocks and mafic rocks with weak or no Eu anomalies. Apatite-poor samples have the lowest REE concentrations (Fig. 8A) and HREE abundances are close to chondrite values. Figure 8B shows the chondrite-normalized REE patterns for various rock types of QMUI, occurring in different parts of the stratigraphic sequence.

Despite minor differences mafic rocks show similar REE patterns (Fig. 8B). Most show flatter REE patterns ($La_N/Yb_N = 2.6–13$) with positive Eu anomalies ($Eu/Eu^* = 1.2–3.7$) and low abundances of REE (total REE = 19–57 ppm) when compared with apatite-rich ultramafic rocks. Mylonitic granite/quartzo-feldspathic gneiss (e.g., TM68) displays convex upwards patterns with negative Eu anomaly ($Eu/Eu^* \sim 0.6$), high LREE/MREE ratio ($La_N/Sm_N \sim 5.5$). In the ultramafic rocks apatite is the predominant reservoir for the REE (Fig. 7B) while small differences in abundances and shape of REE patterns in the mafic rocks are controlled largely by clinopyroxene content. Primitive mantle-normalized trace elements abundances are illustrated in Fig. 8C.

Discussion and conclusions

The Qareaghaj mafic-ultramafic intrusion (QMUI) is a relatively small igneous body when compared to other intracratonic mafic layered complexes or massif-type anorthosites. The mafic rocks of the intrusion have simple mineral assemblages (plagioclase + clinopyroxene + ilmenite) and are locally metamorphosed to amphibolite and foliated gabbro. Based on field relationships, petrography and bulk composition (Tables 1, 7), the various mafic rocks, including coarse-grained gabbro, microgabbro and amphibolite, are co-magmatic and the variation in their bulk composition can easily been explained by modal variations in plagioclase and clinopyroxene. The microgabbros which are characterized by higher Cr, Ni, Mg (Table 7) and An-richer plagioclase (Table 4) than the coarse gabbros and amphibolites can be considered as representative of the parent magma for the mafic rocks of QMUI. On the basis of the Eu/Eu^* values (*Markl*, 2001), microgabbros ($Eu/Eu^* \approx 1$) represent frozen melt whereas coarse-grained gabbros ($Eu/Eu^* > 1$) are cumulates.

In contrast, the ultramafic rocks of the QMUI clearly have unusual mineral assemblage (Table 1) and bulk composition (Table 7); they are classified as Fe-Ti-P-rich rocks (FTP). Considering (1) the very close spatial association of the FTP and the gabbros (Fig. 2A) (2) the enrichment of all plagioclase-incompatible elements and negative Eu-anomaly in FTP (Fig. 8A and B), (3) the sub parallel REE patterns of FTP and gabbros (Fig. 8B) and (4) similar clinopyroxene composition in both rock types (Fig. 5A) we hypothesize that FTP of QMUI, represent residual melts derived from a gabbroic parental magma by extreme fractionation of plagioclase. The FTP melt as a late stage product of gabbro crystallization was able to intrude partially or completely consolidated gabbros. The presence of gabbro xenoliths and plagioclase xenocrysts in the FTP (Fig. 2C) also supports the intrusive nature of FTP.

However, when considered in detail, a direct link between FTP and their gabbroic hosts seems to be problematic. The reasons include: (1) a very different mineral assemblage, in particular the absence of olivine, apatite and magnetite even in trace amounts in the gabbros, and primary plagioclase in FTP (Table 1), (2) presence of two Fe-Ti oxides (ilmenite + magnetite) in FTP rocks but ilmenite as the only oxide phase in the gabbros, (3) low concentrations of REE and weak or lacking Eu-anomalies in apatite-poor ultramafic rocks compared to the gabbros (Fig. 8A). If we assume that the mafic and ultramafic rocks are indeed comagmatic, these differences must be explained. *Owens* and *Dymek* (1992) discussed the following models to explain the changes from an ilmenite to an ilmenite + magnetite assemblage in the Labrieville pluton, Quebec, and in related FTP rocks (OAGN): (i) an increase of Fe/Ti ratio at relatively constant fO_2, (ii) a decrease in fO_2 at constant Fe/Ti ratio during differentiation and (iii) reactions involving ilmenite, orthopyroxene, quartz and ulvöspinel without change in fO_2. They concluded that crystallization of ilmenite (Fe $\approx$ Ti) and pyroxene (Fe $\geq$ Ti) seems to result in a decrease of Fe/Ti and also a decrease in fO_2 at constant Fe/Ti ratio should produce abundant Fe-rich silicates in FTP instead of magnetite. In QMUI, the absence of quartz, orthopyroxene and the low modal content of ilmenite in gabbros (Table 1) suggest that such reaction processes have not taken place. Moreover, based on ilmenite composition only (higher Mg and lower Mn in FTP than gabbros, Table 6), the FTP seem to be more primitive than the gabbros. Hence, magmatic fractionation cannot explain the observed differences among the main rock types at QMUI.

Different conditions of crystallization and evolution seem to be necessary to explain the observed differences between FTP and gabbros, involving different magmas with different ranges of fO_2. It is likely that the magma responsible for the formation of FTP was derived from an external source without a genetic link to gabbros. The structural arrangement of FTP as sill-like bodies and layers with sharp and concordant contact to gabbroic host rocks may be due to injection of FTP fractionated melt into previously crystallized gabbros during plastic, high temperature deformation in local shear zones.

The FTP in QMUI consists of many parallel sill-like bodies and sheets. In these rocks most of the Fe-Ti oxides and apatite appear interstitial to other minerals and can be considered as late stage minerals. However, *Duchesne* (1999) noted that the interstitial appearance does not necessarily mean that they are late stage phases; subsolidus grain boundary readjustment can also explain this feature. Moreover oxide and sulfide droplets found in some FTP, classically interpreted as result of immiscibility (e.g., *Force*, 1991), can also be explained by such subsolidus readjustments (*Vernon*, 1976; *Duchesne*, 1999). However, the presence of oxide and sulfide droplets in early crystallized silicates (Fig. 2B–D) at least reveals that these constituents were present early in the evolution of the magmatic system.

In FTP of QMUI dominant ilmenite (mostly as discrete grains) indicates that fO_2 was relatively low. Beside high Ti and fO_2, the phosphorus content of the magma is a further significant factor controlling paragenesis of ilmenite and Ti-magnetite. High P_2O_5 in FTP magma is found to suppress the crystallization of magnetite in favor of ilmenite (*Toplis*, 1994; *McBirney*, 1996; *Zhou* et al., 2005). However, this is not confirmed by the high ilmenite/magnetite ratio in the apatite-poor rocks of QMUI (Table 1). On the other hand phosphorus can enhance the solubility of oxide

components in silicate liquids and thus prohibit saturation in Fe and Ti and result in formation of high grade deposits (*Duchesne*, 1999; *Kärkkäinen* and *Appelqvist*, 1999). With regard to FTP in QMUI where only disseminated and net-texture mineralization are found, we suggest that beside enrichment in Fe, Ti and P in the magma and a relatively high fO_2, other concentration mechanisms such as liquid immiscibility, filter pressing and/or deformation are necessary for the formation of a high grade deposit.

Most FTP in QMUI show planar fabrics (Fig. 2B and C), which may have various origins such as deformation, compaction and magmatic flow (e.g., *Reynolds*, 1985a; *Nicolas*, 1992; *Hunter*, 1987; *McBirney* and *Nicolas*, 1997). A reasonable explanation for the planar fabric in FTP of QMUI is magmatic flow of a crystal mush combined with deformation in shear zones during emplacement of the FTP. In contrast with gabbros, evidence for deformation, such as dislocation or bending in crystals, has not been seen in FTP, since most of the strain is taken up by the liquid matrix (cf., *Nicolas*, 1992).

Most FTP of QMUI appear to be apatite-rich. Rare apatite-poor rocks (~ 5–10% of the ultramafic outcrops) conspicuously show higher Mg# of olivine and spinel (Table 2 and Fig. 3) than apatite-rich ones and in some samples (e.g., TM16) MREE and HREE concentrations are close to chondrite values. Thus we think that apatite-poor rocks could be more primitive (less evolved) than apatite-rich ones. Because of the very close field relationships, overall similarity in REE pattern (Fig. 8A) and similarity in bulk composition (except in P_2O_5) derivation of apatite-poor and apatite-rich rocks from different batches from a single magmatic source is reasonable.

The FTP of QMUI show peculiar differences as well as similarities with FTP from other localities. The Mg-rich olivine, high bulk MgO, high ilmenite/magnetite ratio, normal gabbroic host, parallel sill-like bodies and layers, mineral lamination, absence of orthopyroxene and primary plagioclase, and close occurrence of apatite-poor and apatite-rich rocks are some distinct differences. Based on the mineral assemblage, texture and bulk composition (Table 7), FTP of QMUI show similarities with apatite-rich oxide ultramafic rocks of Boulder Lake, Duluth (*Ripley* et al., 1998), net-texture type ilmenite-apatite rich olivine cumulate of the Upper Zone of the Bushveld complex (*Von Gruenewaldt*, 1993), and ferrodiorite of the Rattlesnake body, San Gabriel anorthosite (*Force*, 1991). Apatite-oxide-rich ultramafic rocks of Boulder Lake show most similarities with FTP of QMUI. For nelsonites *Ripley* et al. (1998) proposed immiscibility of Fe-Ti-P-rich liquid but they noted that the origin of spatially associated apatite-oxide-rich rock types is problematic. These may themselves be products of liquid immiscibility, reflecting a continuum in composition with nelsonite as an end member. In contrast to the Duluth complex and other FTP suites, in the QUMI area layered gabbros, ferrogabbro, ferrodiorite, nelsonite, jotunite and anorthosite are not found.

Different hypotheses for the origin and concentration mechanisms of Fe-Ti oxides ($\pm$apatite) have been proposed, e.g. late stage differentiates of anorthosites, coeval mangerite or jotunite (e.g., *Herz* and *Force*, 1978; *Goldberg*, 1984; *Ashwal*, 1993; *McLelland* et al., 1994); immiscible liquids, crystal accumulation, subsolidus recrystallization, and late differentiates of mafic layered intrusions (*Philpotts*, 1967; *Kolker*, 1982; *Morse*, 1982; *Wilmart* et al., 1989; *Von Groenewaldt*, 1993; *McBirney*, 1996; *Ripley* et al., 1998; *Duchesne*, 1999; *Årebäck* and *Stigh*, 2000;

Markl, 2001; *Clark* and *Kontak*, 2004). Although liquid immiscibility is an attractive and popular mechanism, it is unsatisfactory in detail. Residual enrichment processes with accompanying immiscibility may explain pure oxide or oxide-apatite deposits (*Duchesne*, 1999). However, the existence of titanium-oxide-rich immiscible melts is not supported by experimental studies (*Lindsley*, 2001). Fractional crystallization of mafic magma along an iron enrichment trend has been suggested to explain the enrichment of Ti and P in layered mafic intrusions (*Morse*, 1980, 1990; *Lee*, 1996).

As noted by *Zhou* et al. (2005), the enrichment of Fe, Ti and P in magmas may be a primary feature of parental magmas attributable either to the mantle source composition or the process of partial melting; alternatively the more likely mechanism is that FTP magmas formed through fractionation and thus are highly evolved mantle melts. The low Ni and Cr contents in olivine and in the bulk rocks (Tables 2, 7) are consistent with the parental magma of FTP being highly evolved melts.

We suggest that a P-rich ferrobasaltic magma parental to FTP may have formed by crystal fractionation at depth in an open system, not far from the QMUI magma chamber. Further fractionation developed a stratified magma chamber with the early crystallization of olivine cumulate on the floor and apatite-rich melt on its top. The variation in apatite abundance as well as mineral composition (olivine and spinel) are interpreted as a result of the breakdown of the stratified magma chamber and multiple injections of FTP magma into an early gabbroic host during plastic, high temperature deformation (amphibolite). The positive Ti and Nb, and negative Zr anomaly (Fig. 8C) as well as the low contents of U, Th and Hf in FTP of QUMI (Table 7) can not be explained by upper crustal contamination because Zr, U, Th and Hf are typically enriched, and Nb and Ti are depleted in the upper crust (*Taylor* and *McLennan*, 1985). Furthermore, the close similarity between QMUI- and Type B mantle apatite (see Fig. 5B) does not indicate any contamination or metasomatic processes. Further studies about Fe-Ti-P-rich liquid separation and also the effect of phosphorus in the fractionation of ferrobasaltic melts are required to explain whether the FTP in QMUI are linked to an immiscible liquid or represent extreme differentiates of a ferrobasaltic parent magma. Some questions such as contribution of mantle and crustal material to the parental magma, effects of contamination and magma mixing processes can only be adequately addressed in the future when data on the isotopic composition of various rock types of QMUI will be available.

Acknowledgements

Field work was carried out with the support of the Tehran University. The authors are grateful to Stefanie Heidrich, Helmut Schleicher and Peter Stutz (Institute of Mineralogy and Petrology, Hamburg University) for their help during the microprobe analyses, useful discussions and preparation of polished thin sections, respectively. We are particularly indebted to Ibrahim Uysal (Karadeniz Technical University, Turkey) for his help assistance and also for his valuable comments on an early draft of the manuscript. Many friends and colleagues have provided valuable assistance during of this study, but we are particularly indebted to Ali Emamalipour, Abdolnaser Fazlnia, Ahmad Ahmadi, Mahmoud Hojati for their useful discussions and help during field work. We are also grateful to S. Maaloe and B. Robins for their constructive reviews which have significantly improved the manuscript and to *Mineralogy and Petrology* Editor J. G. Raith for his editorial input.

References

Andersen DJ, Lindsley DH (1985) New (and final!) models for the Ti-magnetite/ilmenite geothermometer and oxygen barometer. EOS 66: 416

Årebäck H, Stigh J (2000) The nature and origin of an anorthosite associated ilmenite-rich leuconorite, Hakefjorden Complex, south-west Sweden. Lithos 51: 247–267

Ashwal LD (1993) Anorthosites: Berlin, Heidelberg, New York, Springer-Verlag, p 422

Bishop FC (1980) The distribution of Fe^{2+} and Mg between coexisting ilmenite and pyroxene with applications to geothermometry. Am J Sci 280: 46–77

Buddington AF, Lindsley DH (1964) Iron-titanium oxide minerals and synthetic equivalents. J Petrol 5: 310–357

Clark AH, Kontak DJ (2004) Fe-Ti-P oxide melts generated through magma mixing in the Antauta subvolcanic center, Peru: implications for the origin of nelsonite and iron oxidedominated hydrothermal deposits. Econ Geol 99: 377–395

Crawford AR (1977) A summary of isotopic age data for Iran, Pakistan and India: Memoire Hors Serie, Societe Geologique de France 8: 251–260

Daliran F, Amstutz GC (1991) The magnetite-apatite deposit of Mishdovan. An ''alkali rhyolite'' hosted Kiruna type ore in the Bafq metallotect, east central Iran. Third Mining Symposium, Iran, Vol. 2, pp 263–279 (proceedings)

Davoudzadeh M, Weber Diefenbach A (1986) Contribution to the paleogeography, stratigraphy and tectonics of the upper Paleozoic of Iran. N Jb Geol Paläont, Abh 175: 121–146

Duchesne JC (1999) Fe-Ti deposits in Rogaland anorthosites (South Norway): geochemical characteristics and problems of interpretation. Mineral Deposita 34: 182–198

Dymek HF, Owens BE (2001) Petrogenesis of apatite-rich rocks (nelsonites and oxide-apatite gabbronorites) associated with massif anorthosites. Econ Geol 96: 797–815

Dymek RF (1990) Petrogenetic implications of Ga/Al ratios in massif anorthosites. Geol Soc Am Abstr Programs 22: A300

Emamalipour A, Masoudi J (1996) Titanium and phosphorus prospecting in the Qareaghaj area, NW of Urmia, Iran (in Persian). Ministry of Industries and Mines. Tehran

Force ER (1991) Geology of titanium mineral deposits: Geological Society of America Special Paper 259, p 112

Förster H, Jafarzadeh A (1994) The Bafq mining district in central Iran – a highly mineralized infracambrian volcanic field. Econ Geol 89: 1697–1721

Frost BR, Lindsley DH (1992) Equilibria among Fe-Ti oxides, pyroxenes, olivine and quartz: Part II. Application. Am Mineral 77: 1004–1020

Goldberg SA (1984) Geochemical relationship between anorthosite and associated iron-rich rocks, Laramie Range, Wyoming. Contrib Mineral Petrol 87: 376–387

Haggerty SE (1991) Oxide textures: a mini-atlas. In: *Lindsley DH* (ed) Oxide minerals: petrologic and magnetic significance. Rev Mineral 25: 129–219

Haghipour A, Aghanabati A (1973) Geological quadrangle map of Iran No. A3. Serow sheet, Series 1:250000, Geological Survey of Iran (GSI), Tehran

Hassanipak AA, Ghazi AM (2000) Petrology, geochemistry and tectonic setting of Khoy ophiolite, northwest Iran: implications for Tethyan tectonics. J Asian Earth Sci 18: 109–121

Herz N, Force ER (1987) Geology and mineral deposits of the Roseland district of central Virginia: U.S Geological Survey Professional Paper 1371, p 56

Hunter RH (1987) Textural equilibrium in layered igneous rocks. In: *Parsons I* (ed) Origins of igneous layering. Reidel, Dordrecht, NATO Adv Sci Inst C 196: 473–504

Jiang N, Chu X, Mizuta T, Ishiyama D, Mi J (2004) A magnetite-apatite deposit in the Fanshan alkaline ultramafic complex, Northern China. Econ Geol 99: 397–408

Kärkkäinen N, Sarapää O, Husskonen M, Koistinen E, Lehtimäki J (1997) Ilmenite exploration in western Finland, and the mineral resources of the Kälviä ilmenite deposit. Geol Surv Finland Spec Paper 23: 15–24

Kärkkäinen NK, Appelqvist H (1999) Genesis of a low-grade apatite-ilmenite-magnetite deposit in the Kauhajärvi gabbro, Western Finland. Mineral Deposita 34: 754–769

Kärkkäinen NK, Bornhorst TJ (2003) The Svecofennian gabbro-hosted Koivusaarenneva magmatic ilmenite deposit, Kälviä, Finland. Mineral Deposita 38: 169–184

Kavoshgaran (1996) The laboratory scale processing of titanium and phosphorus minerals of Qareaghaj deposit, Urmia, Iran (in Persian)

Kolker A (1982) Mineralogy and geochemistry of Fe-Ti oxide and apatite (nelsonite) deposits and evaluation of the liquid immiscibility hypothesis. Econ Geol 77: 1146–1158

Kretz R (1994) Metamorphic crystallization. John Wiley & Sons, Chichester, 507 pp

Larsen RB, Brooks CK (1994) Origin and evolution of gabbroic pegmatites in the Skaergaard Intrusion, East Greenland. J Petrol 35: 651–679

Lee CA (1996) A review of mineralization in the Bushveld complex and some other layered intrusions. In: *Cawthorn RG* (ed) Layered intrusions. Amsterdam, Elsevier, pp 103–146

Lepage LD (2003) ILMAT: An Excel worksheet for ilmenite-magnetite geothermometry and geobarometry. Comp Geosci 29: 673–678

Lindsley DH (2001) Do Fe-Ti oxide magmas exist? Geology: yes, experiments: no! In: *Korneliussen A* (ed) Abstracts – GEODE field workshop 8–12th July 2001 on ilmenite deposits in the Rogaland anorthosite province, S. Norway, NGU Report no. 20001.042, p 83

Markl G (2001) REE constraints on fractionation processes of massive-type anorthosites on the Lofoten Islands, Norway. Mineral Petrol 72: 325–351

Markl G, Frost BR, Bucher K (1998) The origin of anorthosites and related rocks from the Lofoten Islands, Northern Norway. I. Field relations and estimation of intrinsic variables. J Petrol 39: 1425–1452

McBirney AR (1996) The Skaergaard intrusion. In: *Cawthorn RG* (ed) Layered intrusions. Amsterdam, Elsevier, pp 147–180

McBirney AR, Nicolas A (1997) The Skaergaard layered series. Part II. Magmatic flow and dynamic layering. J Petrol 38: 569–580

McLelland J, Ashwal Z, Moore L (1994) Composition and petrogenesis of oxide-, apatite-rich gabbronorites associated with proterozoic anorthosite massifs: Examples from the Adirondack Mountains, New York: Contrib Mineral Petrol 116: 225–238

Morimoto N (1989) Nomenclature of pyroxenes. Can Mineral 27: 143–156

Morse SA (1980) Kiglapait mineralogy II: Fe-Ti oxide minerals and the activities of oxygen and silica. J Petrol 21: 685–719

Morse SA (1982) A partisan review of Proterozoic anorthosites. Am Mineral 67: 1087–1100

Morse SA (1990) The differentiation of the Skaergaard intrusion. Discussion of Hunter and Sparks (Contrib Min Petrol. 95: 451–461). Contrib Min Petrol 104: 235

Mücke A (2003) Magnetite, ilmenite and ulvite in rocks and ore deposits: petrography, microprobe analyses and genetic implications. Mineral Petrol 77: 215–234

Mücke A, Younessi R (1994) Magnetite-apatite deposits (Kiruna-type) along the Sanandaj-Sirjan zone and in the Bafq area, Iran, associated with ultramafic and calcalkaline rocks and carbonatites. Mineral Petrol 50: 219–244

Nicolas A (1992) Kinematics in magmatic rocks with special reference to gabbros. J Petrol 33: 891–915

O'Reilly SY, Griffin WL (2000) Apatite in the mantle: implications for metasomatic processes and high heat production in Phanerozoic mantle. Lithos 53: 217–232

Owens BE, Dymek RF (1992) Fe-Ti-P-rich rocks and massif anorthosite: problems of interpretation illustrated from the Labrieville and St-Urbain plutons, Quebec. Can Mineral 30: 163–190

Owens BE, Rockow MW, Dymek RF (1993) Jotunites from the Grenville Province, Quebec: petrological characteristics and implications for massif anorthosite petrogenesis. Lithos 30: 57–80

Philpotts AR (1967) Origin of certain iron-titanium oxide and apatite rocks. Econ Geol 62: 303–315

Reynolds IM (1985a) Contrasted mineralogy and textural relationships in the uppermost titaniferous magnetite layers of the Bushveld complex in the Biektaal area north of Rustenburg. Econ Geol 80: 1027–1048

Reynolds IM (1985b) The nature and origin of titaniferous magnetite-rich layers in the upper zone of the Bushveld complex: a review and synthesis. Econ Geol 80: 1089–1108

Rippley EM, Severson MJ, Hauck SA (1998) Evidence for sulphide and Fe-Ti-P-rich liquid immiscibility in the Duluth Complex, Minnesota. Econ Geol 93: 1052–1062

Severson MJ (1988) Geology and structure of a portion of the Partridge River intrusion: a progress report: Duluth, University of Minnesota, Natural Resources Research Institute, Technical Report NRRI/GMIN-TR-88-08, p 78

Stöcklin J (1974) Possible ancient continental margins in Iran. In: *Burk CA, Drake Cl* (eds) The geology of continental margins. Springer, Berlin Heidelberg New York, pp 873–887

Sun SS, McDonough WF (1989) Chemical and isotopic systematics of oceanic basalts: implications for mantle composition and processes. In: *Saunders AD, Norry MJ* (eds) Magmatism in the ocean basins. Geological Society, London, Special Publications 42, pp 313–345

Taylor SR, McLennan SM (1985) The continental crust: its composition and evolution. Oxford, Blackwell, 312 pp

Tindle AG, Webb PC (1994) PROBE-AMPH: A spreadsheet program to classify microprobe-derived amphibole analyses. Comp Geosci 20: 1201–1228

Toplis MJ, Dingwell DB, Libourel G (1994) The effect of phosphorus on the iron redox ratio, viscosity, and density of an evolved ferro-basalt. Contrib Mineral Petrol 117: 293–304

Vernon RH (1976) Metamorphic processes. George Allen and Unwin, London, p 246

Von Gruenewaldt G (1993) Ilmenite-apatite enrichments in the upper zone of the Bushveld complex: a major titanium-rock phosphate resource. Int Geol Rev 35: 987–1000

Watson TL, Taber S (1913) Geology of the titanium and apatite deposits of Virginia: Virginia Geological Survey Bulletin 3A, 308 pp

Wilmart E, Demaiffe D, Duchesne JC (1989) Geochemical constraints on the genesis of the Tellnes ilmenite deposit, Southwest Norway. Econ Geol 84: 1047–1056

Zhou MF, Robinson PT, Lesher M, Keays RR, Zhang CJ, Malpas J (2005) Geochemistry, petrogenesis and metallogenesis of the Panzhihua gabbroic layered intrusion and associated Fe-Ti-V oxide deposits, Sichuan Province, SW China. J Petrol 46: 2253–2280

Authors' addresses: *M. Mirmohammadi* (e-mail: m_mirsaleh@yahoo.com), *A. Kananian* (e-mail: kananian@khayam.ut.ac.ir), School of Geology, University College of Science, Tehran University, Tehran, Iran; *M. Tarkian* (e-mail: mtark@mineralogie.uni-hamburg.de), Institute of Mineralogy and Petrology, University of Hamburg, Grindelallee 48, D-20146 Hamburg, Germany